NUREG/CR-3679
LA-10041-MS

Los Alamos National Laboratory is operated by the University of California for the United States Department of Energy under contract W-7405-ENG-36.

Calibration and Qualification of the Los Alamos Failure Model (LAFM)

Los Alamos National Laboratory
Los Alamos, New Mexico 87545

NUREG/CR-3679
LA-10041-MS

R7

Calibration and Qualification of the Los Alamos Failure Model (LAFM)

Ralph E. Baars

Manuscript submitted: February 1984
Date published: May 1984

Prepared for
Division of Accident Evaluation
Office of Nuclear Regulatory Research
US Nuclear Regulatory Commission
Washington, DC 20555

NRC FIN No. A7015

Los Alamos National Laboratory
Los Alamos, New Mexico 87545

CONTENTS

FIGURES

TABLES

CALIBRATION AND QUALIFICATION OF THE LOS ALAMOS FAILURE MODEL (LAFM)

by

Ralph E. Baars

ABSTRACT

The analysis procedure is described in detail for use of the LAFM computer code to predict LMFBR fuel pin performance under transient overpower conditions; also, 5 tests for calibration and 13 tests for qualification are analyzed. The times of cladding breach (molten fuel expulsion) were predicted with an average relative error of 5 per cent. An enthalpy of 1112 kJ/kg correlated the peak fuel enthalpies at the time of failure with a standard deviation of 98 kJ/kg. We conclude with a discussion that many varied tests must be analyzed for adequate evaluation of a fuel pin performance code.

I. INTRODUCTION

This document reports on the calibration and qualification of the most recent version of the Los Alamos Failure Model (LAFM) computer code.[1] The LAFM code was developed primarily to predict the time and axial location of fuel expulsion from Liquid Metal Fast Breeder Reactor (LMFBR) fuel pins under transient overpower (TOP) conditions.

II. SUMMARY AND CONCLUSIONS

A procedure was developed for use of the LAFM code to make hypothetical and pretest predictions of fuel pin performance. This procedure was qualified against 13 varied TOP tests conducted in the Transient Reactor Test (TREAT) facility located at the Idaho National Engineering Laboratory and operated by Argonne National Laboratory (ANL). Results of these analyses are given in Sec. VI. Comparisons of calculated and observed temperature transients are presented in the Appendix for all tests analyzed.

On the basis of this work, we have drawn the following conclusions:

- The LAFM code was shown to be qualified for predicting the time of fuel expulsion over a broad range of pin conditions and for ramp rates ranging from 0.50 $/s to 3 $/s, without need to adjust experimental test data.

- The mean peak fuel enthalpy at the time of fuel expulsion was calculated to be 1112 kJ/kg with a standard deviation of 98 kJ/kg (8.8%).

- The predicted location of fuel expulsion for ANL test E6 was 3 cm higher than was observed. For ANL test J1, the axial location of failure was identified as the top of the fuel column; the predicted location was also there. No other comparisons between predicted and observed locations were possible because failure was not predicted for ANL test H5, and the location of expulsion is not known for the other tests analyzed.

- The degree of agreement between observations and predictions varied substantially, although it was deemed acceptable for all tests. We concluded, however, that analysis of very few tests is not adequate to evaluate a fuel performance code such as LAFM.

III. BACKGROUND

The LAFM code originally was developed to analyze the LMFBR TOP fuel pin tests conducted in the TREAT facility and contribute to the understanding of those tests, with the ultimate goal of developing a reliable way to predict the time and location of fuel expulsion for LMFBR core disruptive accident (CDA) analysis. The code has been developed through several versions, some of which were "qualified." This document is devoted to the calibration and qualification of the most recent version.

IV. CODE DESCRIPTION

The LAFM code, as indicated, is aimed primarily at the analysis of TOP events. Some basic assumptions and features underlying the code include

- Axisymmetry.

- Uranium or mixed-oxide fuel (can be changed easily because of modular construction).

- Type 316 stainless steel cladding.

- Tresca criterion for cladding yielding.[2]

- Cladding model accounts for strain hardening, but neither thermal creep nor strain-rate effects are accounted for directly.

- Empirical correlations for retained gas content and release thereof.

- Radial and circumferential fuel cracking models.

- Material properties from the SACRD data base[3] except as noted.

Cladding failure is predicted using any of three sets of empirical correlations coupled with the life fraction rule. All three sets are correlated to fuel-cladding transient tester (FCTT) data on the response of irradiated and unirradiated cladding to a thermal transient while under load. All three sets are stress-rupture type formulations. Two of the sets are Larson-Miller parameter (LMP) correlations: one set is for a heating rate of 5.6 K/s and the other is for a heating rate of 111 K/s. Each has different correlations for different fluence levels, but to a fluence of 6×10^{26} nvt/m^2 ($E > 0.1$ MeV). Some correlations are common to both sets. The third failure model is a single DORN parameter correlation in which heating rate and fluence are parameters. The cladding heating rate is averaged over the last 10 time steps and axially for use in the DORN parameter. The fluence effects are assumed to saturate at 6×10^{26} nvt/m^2 ($E > 0.1$ Mev) for all three correlations.[4,5] Both the LMP and the DORN correlations[4,5] were developed by the Hanford Engineering Development Laboratory (HEDL). The high-fluence-level LMP correlations were recorrelated at Los Alamos.

A modified cavity pressure model is used in LAFM, with the volume based on the sum of volumes of the fuel-cladding gap, the radial and circumferential cracks, the columnar grain porosity, and the central void. The pressure calculated from this model is added to the fuel vapor pressure (based on the maximum fuel temperature) for the overall cavity pressure.

The code provides for axial fuel movement in the sense that fuel relocates to regions of unused central void. In this fashion, the code does not load cladding in an axial node where the central void has been exhausted as long as central void volume is available somewhere. As soon as all central void space has been filled throughout the pin, the calculation ceases and the following message is printed: "Failure imminent due to porosity collapse." This action amounts to an assumption that, once the pin goes "solid," cladding breach will occur instantaneously, or nearly so. So doing avoids significant complications in the coding but may be questionable for very slow transients.

Fuel creep is simulated by using a temperature above which fuel is assumed strengthless. Fuel above this temperature is treated just as if it were molten except that it does not pass through the heat of fusion until the solidus temperature is reached. The feature effectively assumes that the fuel deformation rate under given

temperatures and loads is either so slow as to justify assuming it is zero, or so fast as to constitute a condition of strengthlessness. Thus, the intermediate region where the rate would be neither negligible nor instantaneous is assumed to be so limited that it can be ignored.

The code now has considerable flexibility on boundary heat-transfer options. The available options are as follows:

- Calculate for flowing sodium with or without structure.
- Input coolant temperatures, heat-transfer coefficients, and (if applicable) peak cladding temperatures for use in failure model calculations.
- Calculate response of static capsule, including estimates of thermocouple temperatures, with or without heat loss from outer surface. For this and following options, an annulus of sodium-potassium (NaK) eutectic mixture is assumed between pin and heat sink.
- Input experimental inner static-capsule thermocouple-temperature transients for use as boundary condition.
- Input experimental outer static-capsule thermocouple-temperature transients for use as boundary condition.

It is because of the fuel creep and static-capsule transient response capability that the code needs further calibration and qualification.

V. CALIBRATION

The aim of the calibration procedure is to develop a rationale for determining the input to the analysis of a particular problem that provides all required input and does so in a fashion to minimize subjective opinions and maximize an objective factual approach.

A. Procedure

Required input to the LAFM code includes

- Definition of fuel regions and radial node structure.
- Definition of axial node structure and of mean axial node values of burnup, fluence, relative power, and steady-state power.
- Definition of gap conductance parameters.
- Definition of cold fuel cracking for TREAT tests.
- Determination of plenum pressure.
- Determination of radial power factors.

We relied heavily on the SIFAIL code[6] to perform much of the detailed characterization work. We altered the code so that it defines the region and radial node structures, assuming 4 regions for stress analysis and 15 nodes for heat transfer. The code prints a file suitable for input to LAFM that includes radial dimensions as well as axial arrays for fluence, node length, burnup, relative test power, and steady-state power.

For gap conductance, we used an option in LAFM that calculates the gas conductivity as a function of composition and current gap temperature. The composition of plenum gas is calculated by the SIFAIL code and input to LAFM along with the "jump distance," or residual heat transfer resistance at gap closure expressed as an equivalent gap thickness. The plenum pressure is also calculated by SIFAIL. The axial power profile used for the static capsule tests was based on data in Ref. 7.

Radial power factors are calculated using a method developed for this version of LAFM, as follows. The method presumes that a radial power distribution has been defined for an unirradiated sample of the fuel to be tested or is otherwise available. Assuming that the radial power factor is a function only of the relative fuel mass between the point in question and the outer surface, the radial power factor can be computed for radial nodes of any size or degree of restructuring. To do this, a polynomial of third degree or less is fit to the data as a function of the relative radius squared -- the equivalent of relative mass. With this relationship, the mean power factor for a particular radial node was calculated using the classical definition of a mean value. The coefficients of the polynomial are input to the code, and the code calculates the rest.

Input to characterize cold fuel cracks was developed from data presented at the Specialists' Meeting on Material Dynamics held at Los Alamos Scientific Laboratory in March 1979.[8] Data on cracks and porosity were presented separately. No distinction was made between radial and circumferential cracks and because the measurements were made on transverse cross sections, no measurements of axial cracks were possible. The data were presented as the fraction of area occupied by cracks in each of 10 rings of equal radial increments. Several cross sections were analyzed, including more than one from some pins.

For application to LAFM, the data were grouped into three distinct power levels according to microstructure: high power ($\geq$ 30.0 kW/m), intermediate power (23.0 to 30.0 kW/m), and low power ($\leq$ 23.0 kW/m). The data within each grouping were averaged for corresponding rings, and the results were plotted as shown in Figs. 1, 2, and 3. These data were then translated into crack widths for each of the four LAFM-defined regions as follows:

- For high-power microstructure fuel, the innermost three rings (30%) were assumed to correspond to the columnar grains region, the middle four rings (40%) were assumed to correspond to the equiaxed region, and the outermost three rings (30%) were assumed to correspond to the unrestructured region. The crack fractions were averaged for each of these regions. The crack widths for the LAFM-defined regions then were taken as the crack fraction times the appropriate midregion circumference.

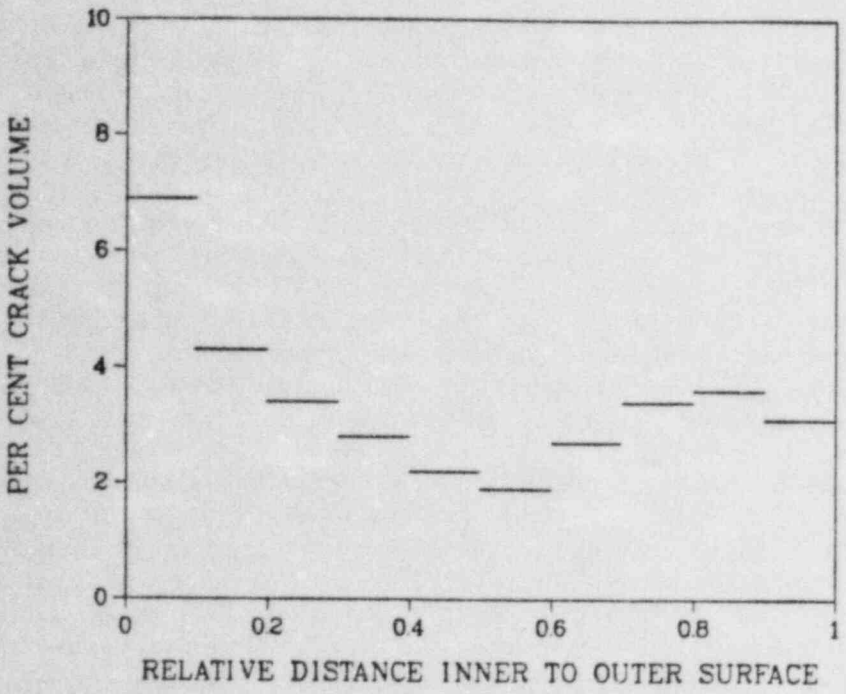

Fig. 1. Fuel crack volumes determined in post-steady-state irradiation examination for 10 equal-thickness fuel zones, for high-power microstructure.

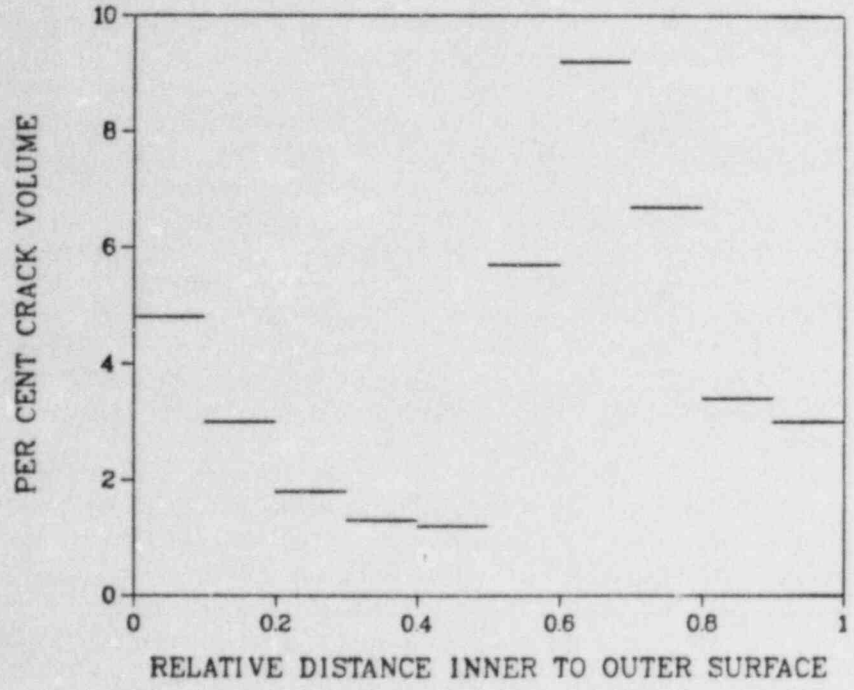

Fig. 2. Fuel crack volumes determined in post-steady-state irradiation examination for 10 equal-thickness fuel zones, for intermediate-power microstructure.

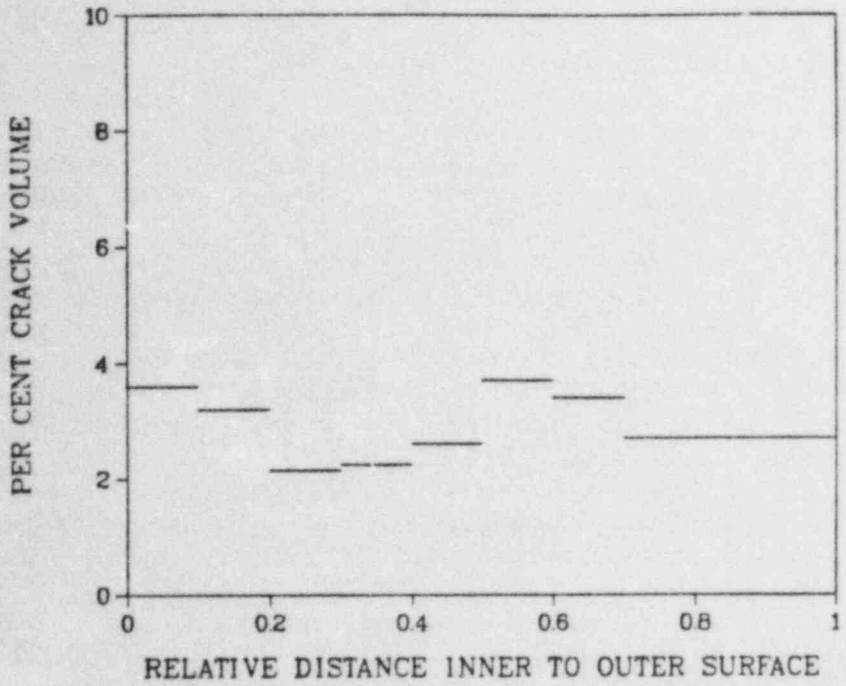

Fig. 3. Fuel crack volumes determined in post-steady-state irradiation examination for 10 equal-thickness fuel zones, for low-power microstructure.

- The intermediate-power microstructure fuel was treated differently because of the circumferential crack, which is confined to this microstructure type. The presence of the circumferential crack is clearly discernable in Fig. 2. The volume of the circumferential crack was determined from Fig. 2, as follows. A smooth curve was drawn between the crack fractions on either side of the circumferential crack peak. The fraction of volume of the affected rings that comprised the circumferential crack was taken as the mean difference between the plotted crack fractions and the smooth curve. The fraction of volume then was applied to the volumes of the affected rings to obtain an actual circumferential crack volume. This volume was translated to a circumferential crack thickness by determining the thickness necessary to produce that volume when applied to the midregion radius of the equiaxed zone. The radial crack widths applicable to regions outboard from the circumferential crack were determined by using the smooth curve. No radial crack widths were determined or input for regions inboard of the circumferential crack because LAFM modeling assumes they are not present.

- For low-power microstructure fuel, there is no differentiation of structure, and the fuel was divided into equal regions. Figure 3 shows there there was no clear dependence of crack fraction on radius, and that the variation of crack fractions was relatively small. Accordingly, the data for all 10 rings were averaged and this single value was used for all regions. The crack widths were determined as above, applying the average crack fraction to the respective midregion circumferences.

All of the irradiated pins analyzed were short (0.34 m) and had little variation in axial power or fuel microstructure. For purposes of crack pattern determination in this analysis, each pin was assumed to have uniform microstructure as defined at the axial midplane, and it was further assumed that there was no variation in crack widths within a given microstructure. Thus, all pins were characterized by one of the three crack width patterns shown in Table I.

Although crack patterns very probably behave in a more sophisticated way than modeled in this analysis, the state of the data and of general code development in our opinion does not warrant more sophisticated treatment.

In keeping with the usual practice in the SIFAIL code, the columnar fuel region is assumed to have a porosity of 2%. The noncolumnar fuel regions are presumed to have the as-fabricated porosity, but this is adjusted as necessary to produce the correct fuel mass for the pin.

TABLE I

CRACK WIDTH PATTERNS FOR TREAT TESTS

Microstructure	Circumferential Crack Thickness (m)	Radial Crack Widths Region (m) 1	2	3	4
Low Power	0.0	0.00005	0.00016	0.00026	0.00038
Intermediate Power	0.00019	0.0	0.0	0.00021	0.00042
High Power	0.0	0.00026	0.00020	0.00026	0.00047

B. Calibration Tests

We analyzed five TOP-tested pins[7,9] for calibration, including two from one test, as identified in Table II. We selected tests to provide a variety of test conditions. None of the tests selected experienced cladding breach. Because of this, some additional information was available upon which to judge the adequacy of results.

An additional word is in order to describe the HUT-L2 loop (flowing-sodium) test. The test, planned and conducted by HEDL, was designed to provide modeling information. Three unirradiated pins were tested, each in its own flow tube, and one of the pins (pin 4) was designed with a smaller than prototypic fuel-cladding gap. Only the total flow to the three flow tubes was measured. We specified individual tube flows for the analysis that totaled to the measured flow, but with individual tube flows adjusted so that approximately the same comparison was obtained between calculated and observed flow tube temperatures for all three flow tubes. The net result was that 36% of the total flow was assumed to pass through flow tube B (pin 4), 33% of the total flow through flow tube A (pin 1), and 30% of the total flow through flow tube C (pin 2). The static capsule test vehicle is discussed further in Section VI.B.

C. Results

Our intention was to use both the test power coupling factors and the value assigned to the temperature of strengthless fuel (TCREEP parameter) as adjustable factors to find the best possible solutions for the five tests analyzed. The initial values used for the power coupling factors were the nominal values reported by the experimentors. A value of 2700 K for TCREEP was based on Ref. 10. Calculated and observed static capsule heat sink temperatures are compared in Figs. A1 through A15 of the Appendix.

D. Discussion

Melt radii were somewhat overpredicted, particularly HUT-37a and HUT-35a, implying power coupling factors that are too high. Some of this overprediction can be attributed to the fact that the predicted radii were at power and temperature while the measured radii were

TABLE II

CALIBRATION TESTS

Test	Type	Pin	Power (kW/m)	Exposure (mWd/kg)	Ramp Rate
HUT-L2-1	Loop	Fresh	Fresh	Fresh	.50 $/s
HUT-L2-4	Loop	Fresh	Fresh	Fresh	.50 $/s
HUT-37A	Capsule	PNL 9-45	18.7	50.0	3$/s
UT-35A	Capsule	PNL 10-20	29.9	54.0	3$/s
HUT-52A	Capsule	PNL 11-28	41.3	51.0	.50 $/s

determined at room temperature. Thus, the predicted radii corrected to the measurement condition could be 5 to 7% smaller.

Hoop strains also were overpredicted but not seriously so. The one poor match on strain (overpredicted for test HUT-52A) most probably was caused by the breakthrough of molten fuel above the top of the fuel column, which raised the upper insulator pellet about 10 mm. No such phenomenon is modeled in the LAFM code.

Very good agreement between calculated and observed temperature transients was obtained, in general, for the static capsule tests. Flow-tube temperatures for the HUT-L2 test were overpredicted. Power coupling factors that were too high, flows that were too low, or some combination thereof could have been responsible. Relatively small adjustments either to power or to flow (well within the uncertainties with which either was known) would have corrected the overprediction.

Cladding breach was predicted for all static capsule tests, where none was observed despite the good thermal agreement for these tests. However, we regard the breach predictions as rather tenuous for HUT-37A and HUT-35A because the life fraction was accumulated entirely in the last half of the power downslope in both cases, reaching peaks of three and four, respectively. Many analysts regard these tests as incipient failures (0.6% strain observed for HUT-37A).[11] We believe that tenuous predictions of failure for these two tests are consistent with the results of the tests. See Sec. VI.D for a further discussion of the significance of life fraction.

For test HUT-52A, the prediction of breach occurred near peak power and appeared to be a conclusive prediction. However, for this test, it has already been pointed out that the breakthrough of molten fuel to raise the upper insulator pellet 10 mm probably minimized the hoop strain that was observed. This behavior almost certainly also minimized the likelihood of cladding breach. Consequently, we do not believe that the prediction of cladding breach for this test significantly affects the evaluation of the code.

Despite indications that powers used in analysis of tests HUT-37A and HUT-35A may have been high and that either too high powers or too low flows were used to analyze the HUT-L2 pins, the deviations of calculated results from observed results were not sufficient in our opinion to warrant further fine tuning of the calibration analyses. Hence, we concluded that nominal power coupling factors and a value of 2700 K for the TCREEP parameter should be used.

VI. QUALIFICATION

Qualification demonstrates that the calculational procedure provides reliable predictions within the desired range of application. In that sense, we can literally qualify the LAFM code only to TREAT TOP tests because essentially no other data exist. Nevertheless, this is a step necessary to demonstrating any code in this field.

A. Procedure

The procedure defined for the calibration phase was used, including the use of nominal power coupling factors and a value of 2700 K for the TCREEP parameter. In addition, it was necessary to calculate the thermal transient in the coolant for the ANL seven-pin bundle tests using a subchannel thermal-hydraulics code. The LACOBRA

code[12] was used for this purpose. The LACOBRA code is the Los Alamos version of the COBRA-IV code[13] and differs from the latter primarily in that it has a more sophisticated, detailed fuel model. The fuel model is very similar to that in the LAFM code, except that it does not perform mechanical analyses.

Essentially identical procedures were used to perform analyses with both LACOBRA and LAFM, and comparisons of fuel temperatures indicate that the two codes yield comparable results. Tables of coolant temperatures and heat-transfer coefficients azimuthally averaged around the pin were input to LAFM as a function of time and axial position. The azimuthally maximum cladding temperatures were also input for use in the cladding-failure criterion calculation.

Axial power profile based on data reported in Ref. 7 was used for the static capsule tests; from Ref. 14 for seven-pin bundle tests E8, H6, and J1; and from Ref. 15 for all other seven-pin bundle tests.

B. Qualification Tests

A total of six HEDL static capsule tests[7,9] (Table III) and seven ANL flowing-sodium, seven-pin bundle tests[14-18] (Table IV) were analyzed for qualification. The matrix of tests used for qualification covers a wider exposure range than did the calibration tests and also differs by including the ANL seven-pin bundle tests.

Brief descriptions of the two test vehicles are in order at this point. The static capsule uses a massive annular nickel heat sink in place of flowing sodium. The test pin is located in the hole in the heat sink and is thermally bonded to the heat sink by an annulus of sodium-potassium (NaK) eutectic mixture. The relation between fuel and cladding temperature fundamentally differs from that in a flowing-sodium system. In general, good simulations to a flowing-sodium system are possible only at one axial location on the capsule, and in "slow" transients, possibly not even at one location. These tests are useful for model development but are not good simulations of the reactor environment.

TABLE III

STATIC CAPSULE QUALIFICATION TESTS

Test	Pin	Power (kW/m)	Exposure (mWd/kg)	Ramp Rate
HUT-37B	PNL 9-54	18.7	50	3 $/s
HUT-36B	WSA 3-28	25.9	108	3 $/s
HUT-32A	PNL 11-47	40.7	50	3 $/s
HUT-57B	PNL 9-34	17.7	47	0.50 $/s
HUT-55A	PNL 10-17	29.2	53	0.50 $/s
HUT-52A	PNL 11-15	40.4	50	0.50 $/s

TABLE IV

SEVEN-PIN BUNDLE QUALIFICATION TESTS

Test	Type	Pin	Power (kW/m)	Exposure (mWd/kg)	Ramp Rate
E6	1 Irr. Pin 6 Fr. Pins	HEDL-NF-056	39.0	46	3 $/s
E7	7 Irr. Pins	HEDL-NF-104	33.5	42	3 $/s
E8	7 Irr. Pins	PNL 10-28	29.9	54	3 $/s
H4	1 Irr. Pin 6 Fr. Pins	HEDL-NF-051	32.8	54	0.50 $/s
H5	1 Irr. Pin 6 Fr. Pins	PNL 11-25	26.2	33	0.50 $/s
H6	7 Irr. Pins	PNL 10-28	30.8	54	0.50 $/s
J1	7 Irr. Pins	ZP-063	26.2	78	0.10 $/s

The seven-pin bundle tests as conducted by ANL provide a flowing-sodium and faithful geometric environment, but have many drawbacks as fuel pin mechanics tests. In their defense, the tests were designed primarily to provide information on postexpulsion phenomena, not fuel pin mechanics information. There are two primary problems with the tests as providers of fuel pin failure information. The integral pump used with the vehicle lies alongside the test section and causes a pronounced azimuthal power variation, not only across the bundle but also across the individual peripheral pins. This azimuthal power variation causes both pin and bundle bowing, and also leads to off-center fuel melting in the peripheral pins. These effects, along with edge hydraulic effects between the fluted tube and the test bundle, substantially complicate and inevitably increase the uncertainty in the test analysis.

The second problem with these tests for fuel pin mechanics purposes is that there is no reliable way to identify which pin fails first and expels molten fuel. It is conventional to assume that the center (irradiated) pin in the bundles with fresh peripheral pins fails first, and that the highest power peripheral pin fails first in the bundles of seven irradiated pins. The convention was followed in these analyses.

C. Results

Observed and predicted cladding breach times are compared in Table V. For this comparison, molten fuel expulsion and cladding breach were assumed to occur simultaneously.

Calculated values of peak cladding hoop strain, peak fuel enthalpy, and peak fuel liquidus fraction are tabulated in Table VI. Comparisons of predicted and observed temperatures for the static capsule tests are shown in the Appendix in Figs. A16 through A45. Comparisons of observed and predicted flow tube and outlet coolant temperatures for the seven-pin bundle tests are shown in the Appendix in Figs. A46 through A63.

TABLE V

COMPARISON OF OBSERVED AND PREDICTED
TIMES OF CLADDING BREACH

Test	Cladding Breach Times (s) Observed	Predicted
HUT-37B	0.87	0.86
HUT-36B	0.62	0.61
HUT-32A	0.7	0.72
HUT-57B	4.72	4.36
HUT-55A	3.25	3.24
HUT-52B	3.62	3.40
E6	0.575	0.57
E7	0.50	0.55
E8	0.50	0.55
H4	0.99	----
H5	1.91	----
H6	2.63	2.83
J1	2.99	3.16

The axial location of fuel expulsion is known with reasonable certainty for only three of the tests: seven-pin bundle tests E6, H5, and J1 (see Ref. 19). Unfortunately, no failure prediction was obtained for H5. For E6, the observed location was at X/L of 0.7 as compared with a predicted location of X/L of 0.79. For J1, both observed and predicted locations were the top of the fuel column.

TABLE VI

CALCULATED VALUES OF SELECTED PARAMETERS
FOR QUALIFICATION TESTS

Test	Peak Hoop Strain (%)	Peak Fuel Enthalpy (kJ/kg)	Peak Fraction[a] of Fuel in Liquid Phase
HUT-37B	0.87	1123.0	0.61
HUT-36B	0.81	1120.1	0.62
HUT-32A	0.73	1222.8	0.78
HUT-57	1.00	1073.7	0.49
HUT-55A	0.46	1088.7	0.51
HUT-52B	1.10	1277.7	0.73
E6	1.37	1204.2	0.69
E7	0.18	1142.0	0.63
E8	0.49	1116.2	0.57
H4	$\leq$0.1	899.0	0.22
H5	$\leq$0.1	874.1	0.18
H6	0.48	1041.1	0.47
J1	0.30	1042.8	0.50

[a]The fraction reported is the fraction of fuel mass in the liquid phase; it is not the same as the areal melt fraction, which is the square of the radius of the solidus isotherm relative to the outer fuel radius.

D. Discussion

A perusal of Table V shows that excellent agreement was obtained between the predicted times of cladding breach and the observed times of fuel expulsion, excepting tests H4 and H5. The average error between predicted and observed times of failure (relative to the elapsed time between the start of the simulated transient and the event) was 5%, with extremes ranging from 1 to 14%. This expresses the excellent agreement quantitatively. The relative error was calculated as follows:

$$E_r = \frac{T_p - T_o}{T_o - T_s} ,$$

where
E_r = relative error,
T_p = predicted time of cladding breach,
T_o = observed time of molten fuel expulsion, and
T_s = time at start of simulated transient (spike).

In the two tests for which cladding breach was not predicted (H4 and H5), peak life fractions of 10 and 15%, respectively, were predicted. We believe these life fractions represent near misses. Another way to place these results into perspective is to consider how these predictions would be regarded if they applied to a test design. If it were important to avoid cladding breach (molten fuel expulsion) in the test, predicted life fractions of 10% or more would probably necessitate redesign of the test to reduce the probability of breach. This is not to downgrade desirability of predicting the breach if one were observed, but rather to point out that the life fraction represents several processes that are basically stochastic in nature, and that the life fraction represents shades of probability. Breach is a real possibility at 10%, although not likely, and is not guaranteed at a life fraction of 200 or 300%, although likely.

H5 was a particularly interesting test in that it is virtually the only test in which cladding breach occurred with some fuel expulsion, yet the bundle was not destroyed. In particular, the central irradiated pin was recovered largely intact. The failure site was clearly identifiable, and melt radii and diameter measurements were possible.[16] The calculated peak axial midplane solidus melt radius and hoop strain were 1.58 mm and nil, respectively, as compared with 1.22 mm and about 0.2% measured, respectively. Coupled with excellent agreement between observed and predicted outlet coolant temperatures (Fig. A56), these results seem to make an incorrect power coupling unlikely.

The lack of a cladding breach prediction for the H4 test was equally puzzling. Good agreement between observed and predicted temperatures was obtained both for the fluted tube at axial midplane and for the outlet coolant (see Figs. A53 and A55). However, predicted

temperatures were 50- to 100-K low for the fluted tube near the top of the fuel column (Fig. A54). This discrepancy could explain the lack of a failure prediction; however, this temperature cannot be increased while preserving agreement for the outlet coolant temperature. Alternatively, in the absence of fuel melt and cladding strain measurements, the possibility of both low apparent power coupling and measured temperatures cannot be ruled out. The calculated values of liquidus fuel melt fraction and of hoop strain seem low, implying too low power. Finally, the models and/or material properties may not represent this particular test pin satisfactorily. Thus, the lack of failure prediction may be due to some effect of the asymmetric power distribution, some uncertainty in measured test conditions, some inadequacy in the models or material properties, or some combination thereof. In short, we conclude that tests H4 and H5 may simply lie at the edge of probable behavior.

The comparisons between observed and predicted temperatures shown in the Appendix demonstrate excellent agreement for the static capsule tests. Generally good agreement was obtained also for the seven-pin bundle tests, although less good agreement than for the static capsule tests. Significant deviations are apparent in some cases. The quality and number of comparisons varied significantly from test to test. Comparisons for outlet coolant temperatures were available for all seven-pin bundle tests, and also for two or more locations on the fluted tube for tests H4, H6, E8, and J1.

Table VI shows that the calculated peak fuel enthalpies for all tests (except H4 and H5) group closely. Including all tests but H5, the mean value is 1112 kJ/kg, with a standard deviation of 98 kJ/kg. We exclude H5 from this formulation because it appeared that only one to two grams of fuel were expelled from the central pin and that hot, soft fuel rather than molten fuel was extruded out of the pin. On the basis that this does not constitute the molten fuel expulsion that is of concern in CDAs, the test was excluded. No such reason can be cited for H4. Obviously, a much tighter correlation would be possible without H4.

We believe that this correlation should be of value to the LMFBR community. For cases where a best estimate is desired, use of the mean value for a fuel expulsion criterion would be suggested. The mean value minus two or three standard deviations could be used as a guide for situations where it is necessary to show very low likelihood of molten fuel being expelled, as in design-basis TOP events.

The mean value of the mass fraction of fuel in the liquid phase was calculated to be 57% for the observed times of fuel expulsion. The standard deviation was 15%. This also is based on all tests but H5, which was excluded for the reasons given above. This formulation provides some basis for the 50% melt fraction that has been used for many years in CDA analysis. The melt criterion could be used similarly to that suggested above for the enthalpy criterion.

No attempt was made to correlate the calculated peak hoop strains. It is noted that they ranged from 0.18 to 1.37%. This range can be used as a guide to check validity of the life fraction calculation for irradiated pins. Predictions of breach with little or no plastic strain should be suspect, as should lack of a breach prediction with strains much over 2% or so.

Of the 13 tests analyzed, the axial location of failure was well established for only 3. Of these, no failure prediction was obtained for one (H5). Of the remaining two, the predicted location agreed within 3 cm for one (E6) and within 1 cm for the other (J1). While this agreement is encouraging, many more such comparisons are required before the LAFM code can be considered qualified for predicting the location of fuel expulsion.

We conclude that the results of analysis of the qualification tests show that the LAFM code on the average satisfactorily predicts results for available tests. We further conclude that it is probably unrealistic to expect any deterministic code, including LAFM, to provide invariably accurate predictions for all situations. Finally, it seems apparent that to evaluate any code against data, a considerable volume of cases must be analyzed for a valid evaluation.

These conclusions have not yet been shown to apply to unirradiated or very low burnup pins. Use of enthalpy, melt, or strain results for such pins is not recommended.

REFERENCES

1. P. K. Mast, "The Los Alamos Failure Model (LAFM): A Code for the Prediction of LMFBR Fuel Pin Failure," Los Alamos Scientific Laboratory report LA-7161-MS (March 1978).

2. T. H. Lin, Theory of Inelastic Structures (John Wiley and Sons, Inc., New York, 1968).

3. N. M. Greene, V. M. Forsberg, G. B. Raiford, J. N. Anwood, J. F. Manneschmidt, and G. F. Flanagan "SACRD - A Data Base for Fast Reactor Safety Computer Codes - Version 81," Oak Ridge National National Laboratory report ORNL/CSD-86 (May 1982).

4. G. D. Johnson and C. W. Hunter, "Mechanical Behavior of Fast Reactor Fuel Pin Cladding Subjected to Simulated Overpower Transients," Hanford Engineering Development Laboratory report HEDL-TME 78-13 (June 1978).

5. G. D. Johnson, J. L. Straalsund, and G. L. Wire, "A New Approach to Stress-Rupture Data Correlation," Materials in Science and Engineering 28, 69-75 (1977).

6. D. R. Wilson and D. S. Dutt, "SIFAIL: A Subprogram to Calculate Cladding Deformation and Damage for Fast Reactor Fuel Pins," Hanford Engineering Development Laboratory report HEDL-TME 79-34 (May 1979).

7. R. E. Baars, G. E. Culley, R. T. Davis, R. G. Henderson, and J. H. Scott, "Base Technology FSAR Support Document-Prefailure Transient Behavior and Failure Threshold Status Report: January

1975," Hanford Engineering Development Laboratory report HEDL-TME 75-47 (November 1975).

8. G. H. Fox and E. H. Randklev, "Fuel Crack Volume Predictions and Measurements," in "Proc. of Specialists' Workshop on Predictive Analysis of Material Dynamics in LMFBR Safety Experiments. March 13-15, 1979," Los Alamos Scientific Laboratory report LA-7938-C (July 1979).

9. R. E. Baars, T. Hikido, and J. E. Hanson, "Fast Reactor Fuel Pin Performance Requirements for Off-Normal Events," Proceedings of International Conference on Fast Breeder Reactor Fuel Performance, Monterey, CA, March 5-8, 1979, American Nuclear Society, La Grange, IL, pp. 155-165 (1979).

10. O. D. Slagle, "Deformation Behavior of UO_2 Above 2000°C," Hanford Engineering Development Laboratory report HEDL-TME 79-37 (September 1979).

11. R. E. Baars, "HEDL Empirical Correlation of Fuel Pin TOP Failure Threshold Status 1976," Proceedings of International Meeting on Fast Reactor Safety and Related Physics, Chicago, IL., October 5-8, 1976, National Technical Information Service, Springfield, VA, pp. 1663-1672 (1976).

12. J. L. Tomkins and P. K. Mast, "LACOBRA/LAFM Analysis of TREAT Test H6," Trans. Am. Nucl. Soc. 34, 514-515 (1980).

13. C. W. Stewart, C. L. Wheeler, R. J. Cena, C. A. McMonagle, J. M. Cuta, and D. S. Trent, "COBRA-IV: The Model and the Method," Battelle Pacific Northwest Laboratories report BNWL-2214 (July 1977).

14. R. Simms, R. K. Lo, W. F. Murphy, G. S. Stanford, and A. B. Rothman, "Transient-Overpower Test E8 on FFTF-Type Low-Power-Irradiated Fuel," Argonne National Laboratory report ANL-77-93 (December 1977).

15. R. C. Doerner, W. F. Murphy, G. S. Stanford, and P. H. Froehle, "Final Report of Fuels Dynamics Test E7," Argonne National Laboratory report ANL-77-25 (April 1977).

16. L. W. Dietrich, R. C. Doerner, T. H. Hughes, and A. E. Wright, "Summary and Evaluation of Fuel Dynamics Transient Overpower Experiment Status, 1974," Argonne National Laboratory report ANL 77-44 (June 1977).

17. R. J. Page, A. B. Rothman, K. J. Schmidt, C. L. Fink, R. W. Mouring, R. K. Lo, P. H. Froehle, and E. W. Johanson, "TREAT TOP Test H6 - Preliminary Results," Trans. Am. Nucl. Soc. 28, 481-482 (1978).

18. R. J. Page, A. B. Rothman, G. E. Marsh, K. J. Schmidt, F. L. Hooper, C. August, E. Johanson, G. Larsen, and P. H. Froehle, "Results from the J1 Low Ramp Rate TREAT Experiment," Trans. Am. Nucl. Soc. 34, 545-546 (1980).

19. R. J. Page, W. F. Murphy, and J. W. Holland, "The Axial Location of Cladding Failure During a Slow Transient Overpower TREAT Test," Trans. Am. Nucl. Soc. 44, 324-325 (1980).

APPENDIX

The Appendix is devoted to graphical comparisons of observed and predicted temperatures. Comparisons for the calibration tests are shown in Figs. A1 through A15. Comparisons for the qualification tests (Figs. A16 through A63) follow the comparisons for the calibration tests.

The tests for which comparisons are shown are for two broad categories — those conducted in flowing sodium (E6, E7, E8, H4, H5, H6, and J1) (Figs. A46 through A63) and those conducted in static-capsule test vehicles (Figs. A1 through A45). A discussion of features of the seven-pin bundle tests (the last-named seven tests above) and of the static-capsule tests is given in Sec. VI.B. The temperatures compared for the flowing-sodium tests were flow tube and/or outlet temperatures, with the axial location of measurement and the number of measurements varying from test to test. Digital listings of temperatures for some of the seven-pin bundle tests were not available, and it was necessary to determine points from plots of measured temperatures for such tests. In such cases, the measured temperatures are smoothed representations, and the comparisons are not as high quality as for the other tests.

In the static-capsule tests, temperatures were measured at axial locations 12.7 mm (0.5 in.) from either end of the fuel column, 63.5 mm (2.5 in.) from either end of the fuel column, and at axial midplane. Temperatures were measured at each of these axial locations at a point recessed nominally 0.6 mm (0.023 in.) into the inner surface of the nickel heat sink. Two such measurements, separated azimuthally by 180°, were made at axial midplane. In addition, the outer heat sink surface temperature was measured at the three axial locations closest to midplane.

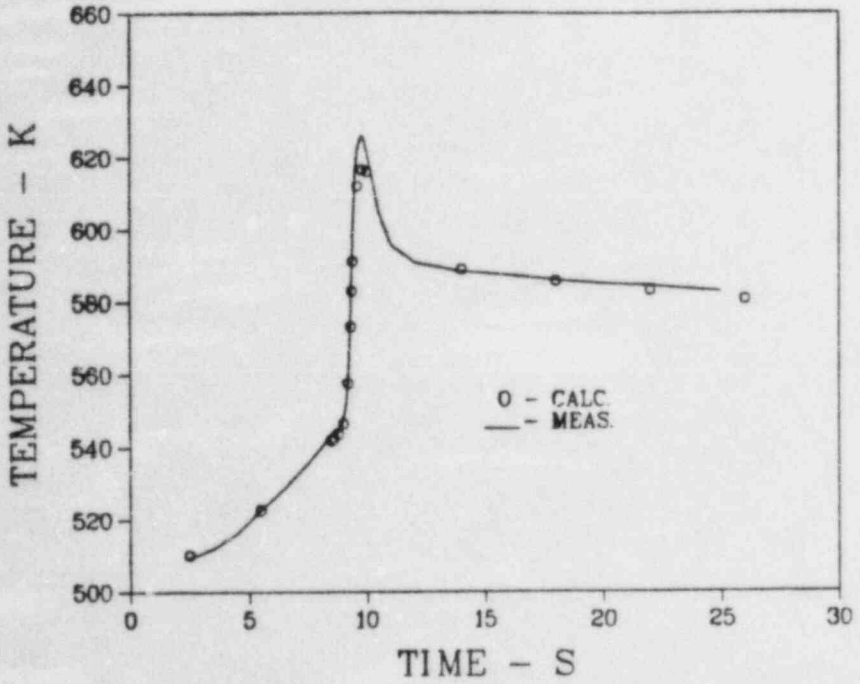

Fig. A1. Comparison of observed and predicted temperatures for HEDL test HUT-37A at an axial location 12.7 mm (0.5 in.) above the bottom of the fuel column.

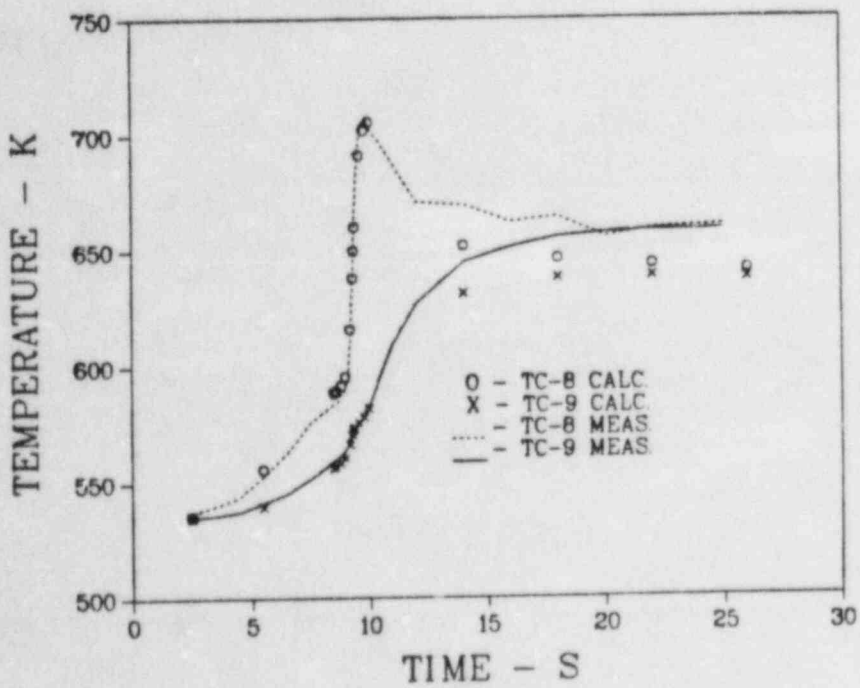

Fig. A2. Comparison of observed and predicted temperatures for HEDL test HUT-37A at an axial location 63.5 mm (2.5 in.) above the bottom of the fuel column.

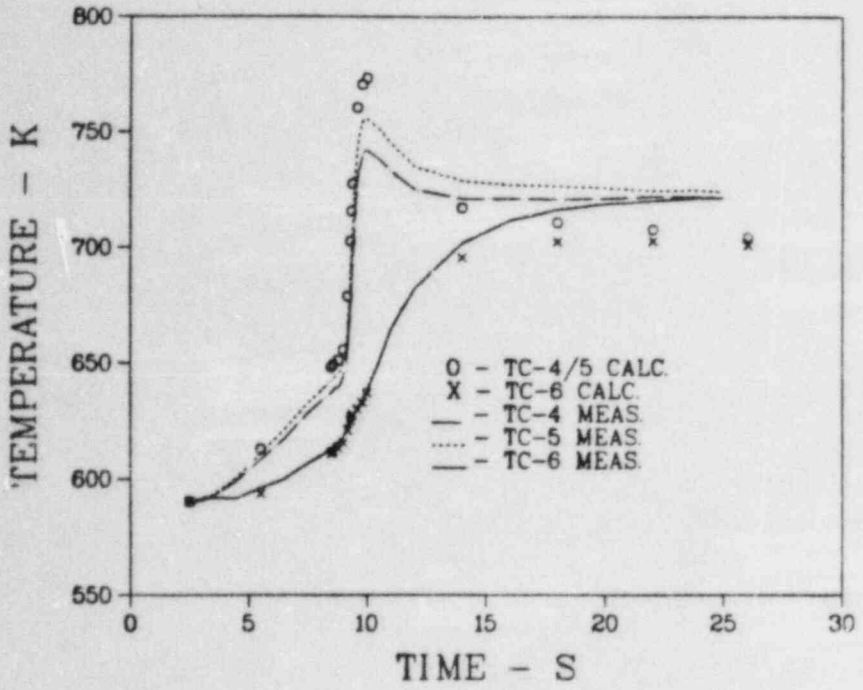

Fig. A3. Comparison of observed and predicted temperatures for HEDL test HUT-37A at axial midplane of the fuel column.

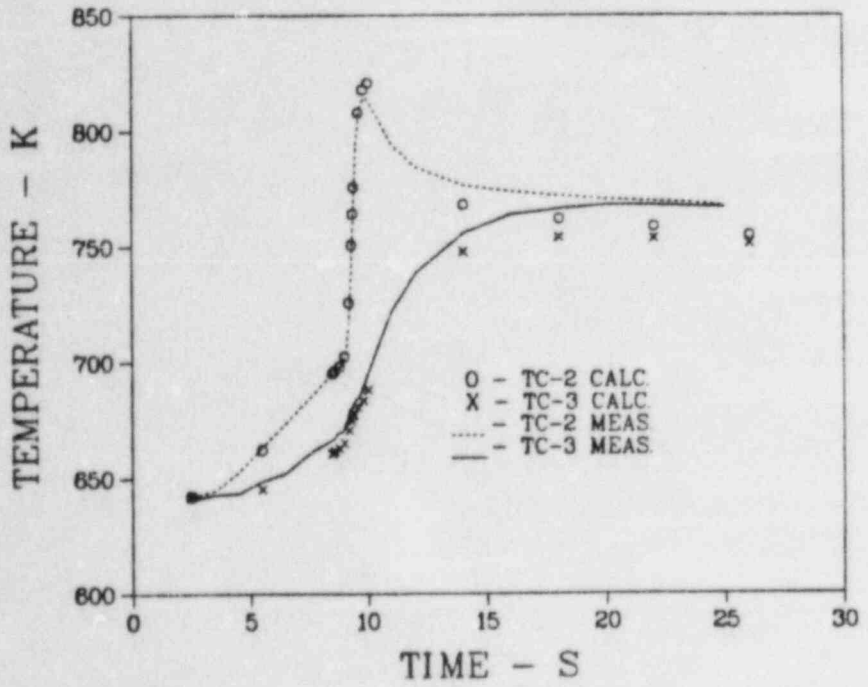

Fig. A4. Comparison of observed and predicted temperatures for HEDL test HUT-37A at an axial location 279 mm (11 in.) above the bottom of the fuel column.

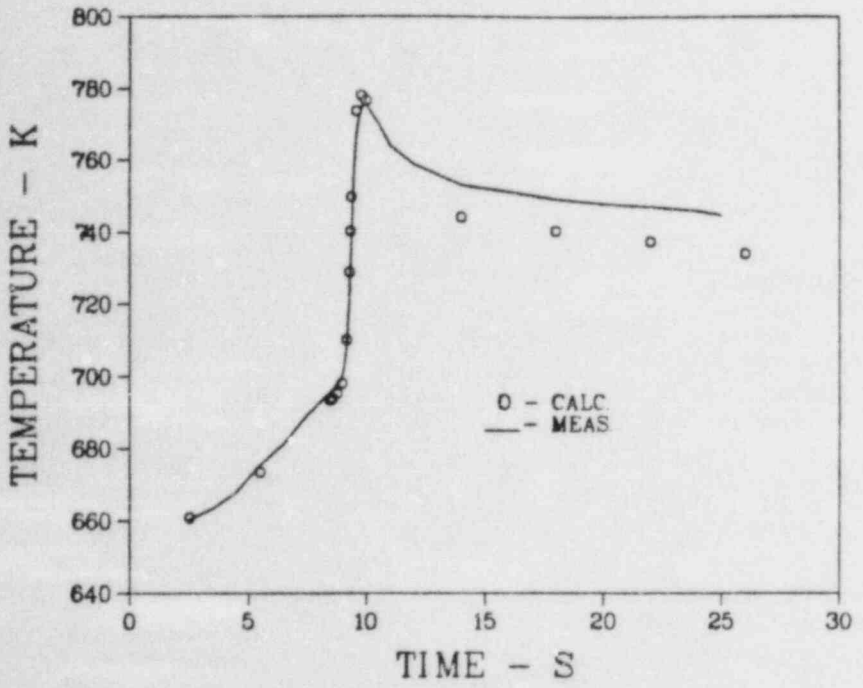

Fig. A5. Comparison of observed and predicted temperatures for HEDL test HUT-37A at an axial location 330 mm (13 in.) above the bottom of the fuel column.

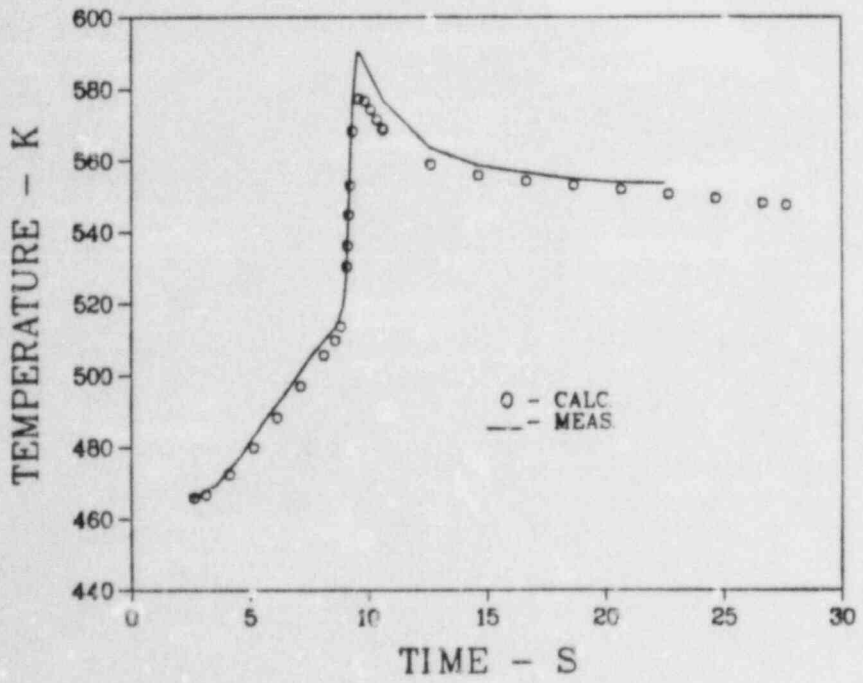

Fig. A6. Comparison of observed and predicted temperatures for HEDL test HUT-35A at an axial location 12.7 mm (0.5 in.) above the bottom of the fuel column.

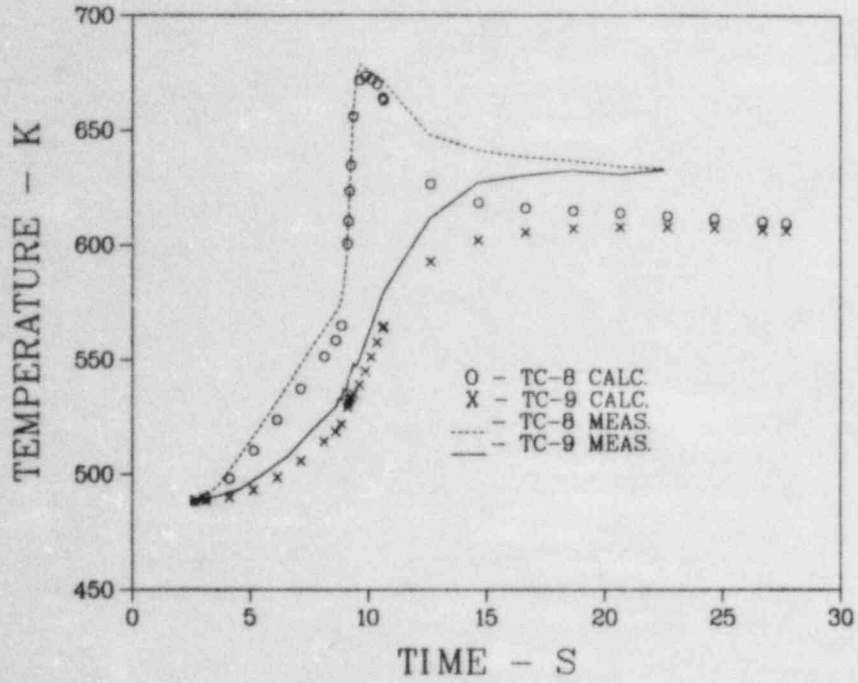

Fig. A7. Comparison of observed and predicted temperatures for HEDL test HUT-35A at an axial location 63.5 mm (2.5 in.) above the bottom of the fuel column.

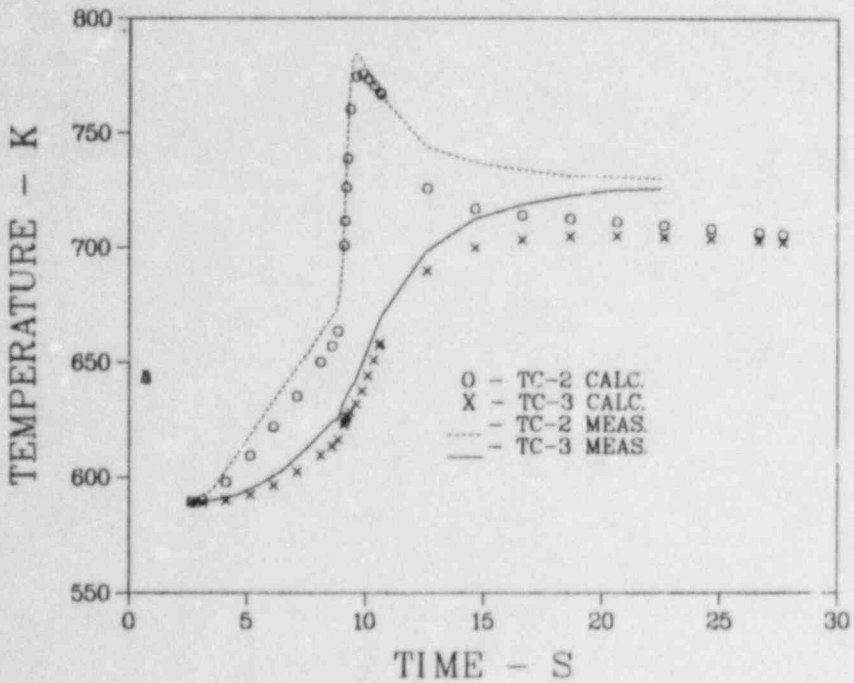

Fig. A8. Comparison of observed and predicted temperatures for HEDL test HUT-35A at axial midplane of the fuel column.

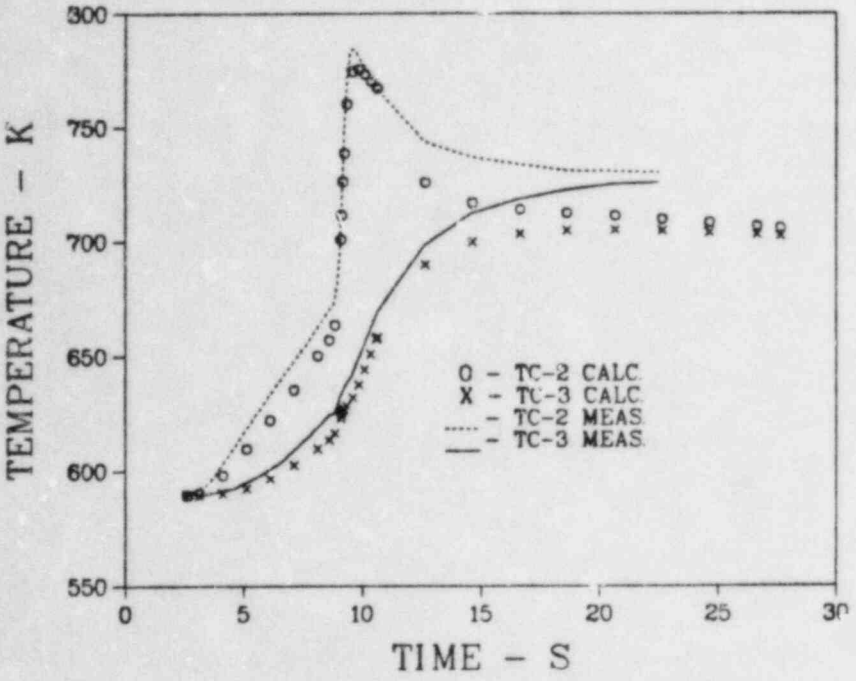

Fig. A9. Comparison of observed and predicted temperatures for HEDL test HUT-35A at an axial location 279 mm (11 in.) above the bottom of the fuel column.

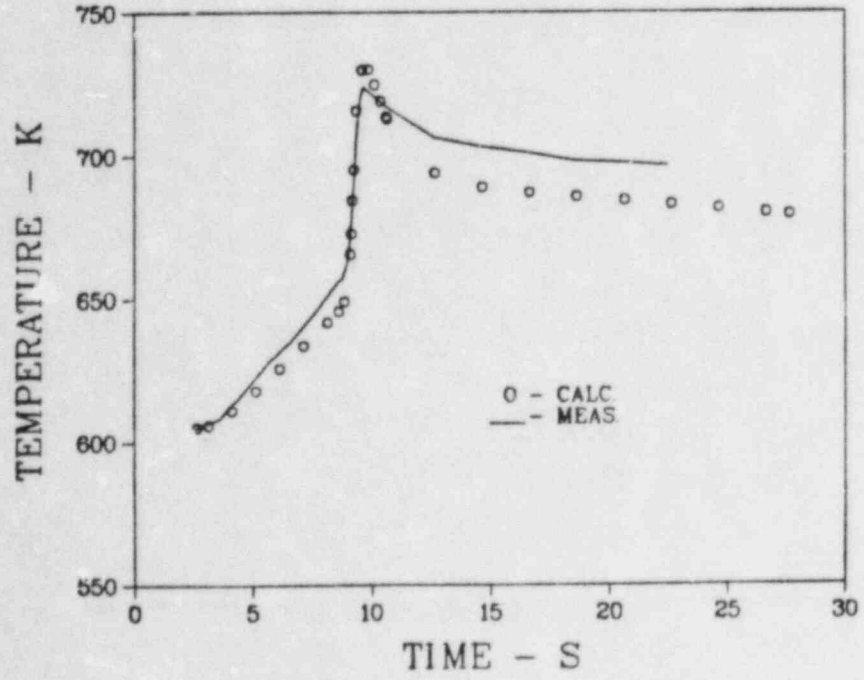

Fig. A10. Comparison of observed and predicted temperatures for HEDL test HUT-35A at an axial location 330 mm (13 in.) above the bottom of the fuel column.

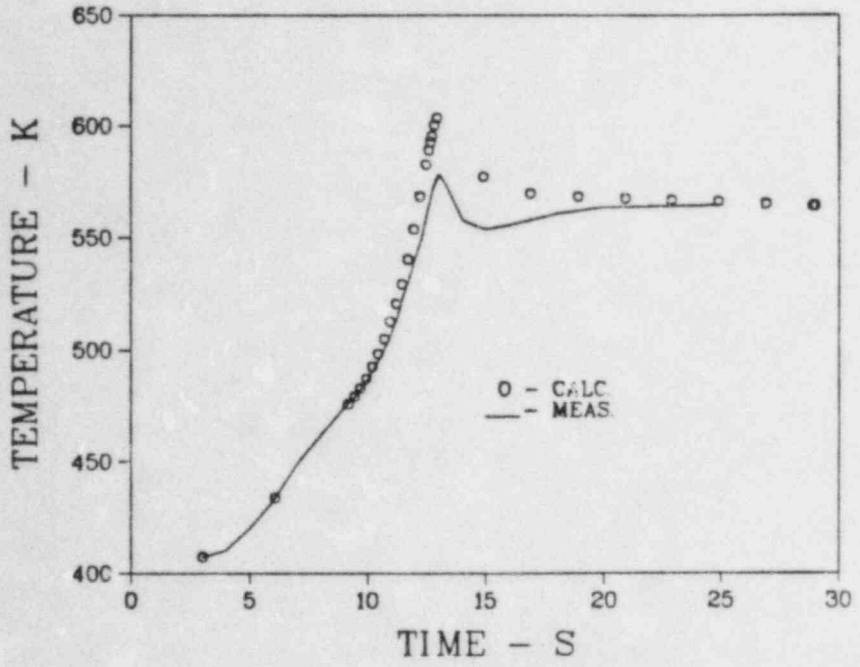

Fig. A11. Comparison of observed and predicted temperatures for HEDL test HUT-52A at an axial location 12.7 mm (0.5 in.) above the bottom of the fuel column.

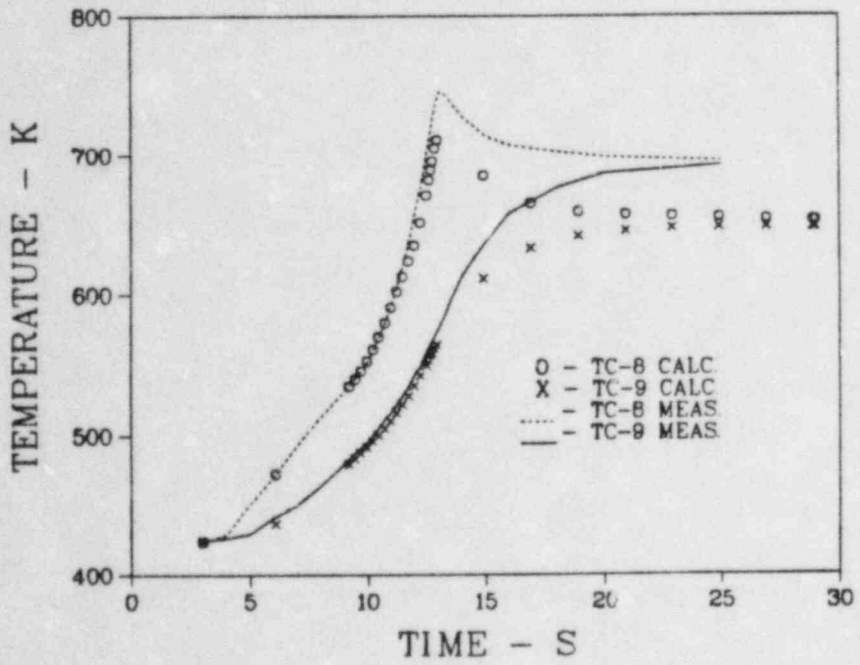

Fig. A12. Comparison of observed and predicted temperatures for HEDL test HUT-52A at an axial location 63.5 mm (2.5 in.) above the bottom of the fuel column.

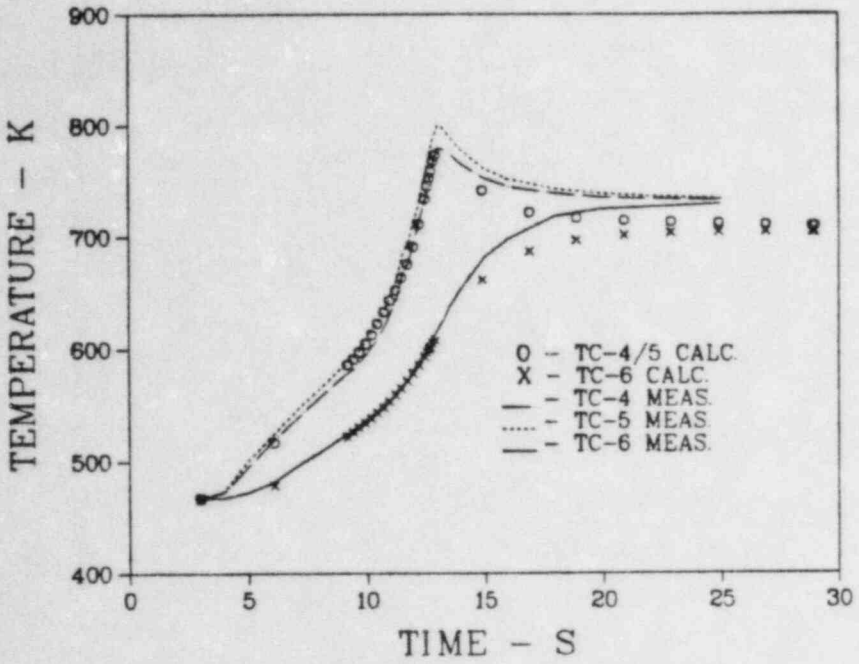

Fig. A13. Comparison of observed and predicted temperatures for HEDL test HUT-52A at axial midplane of the fuel column.

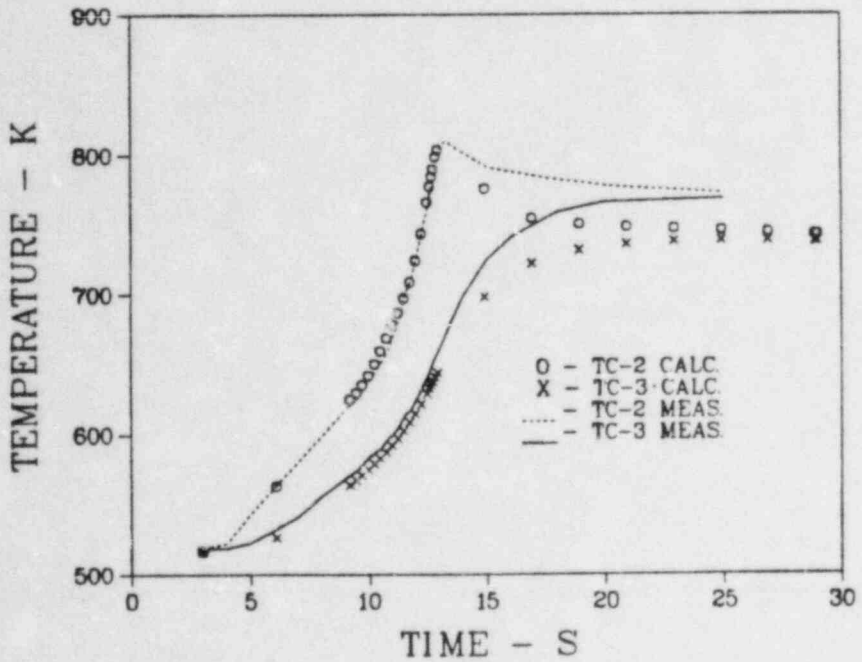

Fig. A14. Comparison of observed and predicted temperatures for HEDL test HUT-52A at an axial location 279 mm (11 in.) above the bottom of the fuel column.

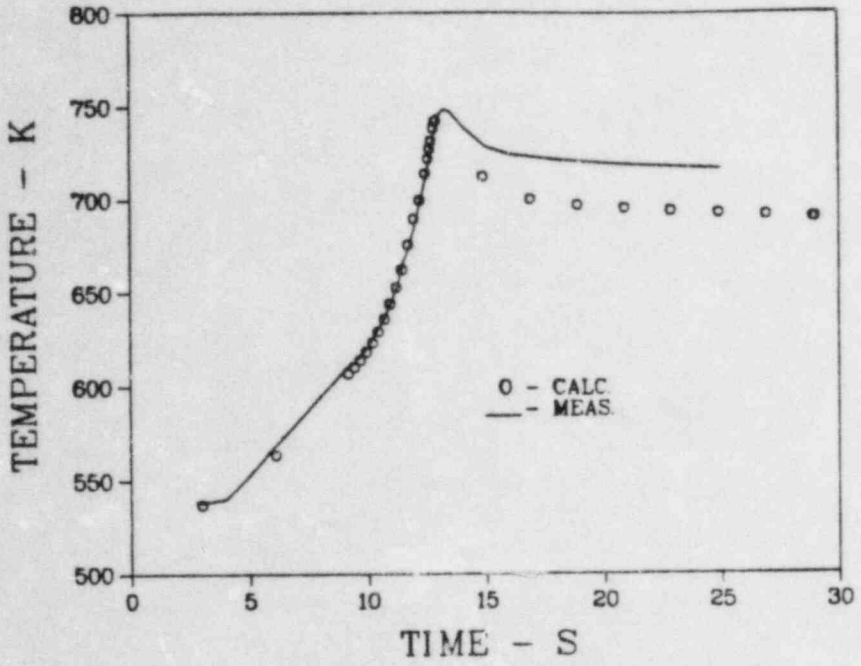

Fig. A15. Comparison of observed and predicted temperatures for HEDL test HUT-52A at an axial location 330 mm (13 in.) above the bottom of the fuel column.

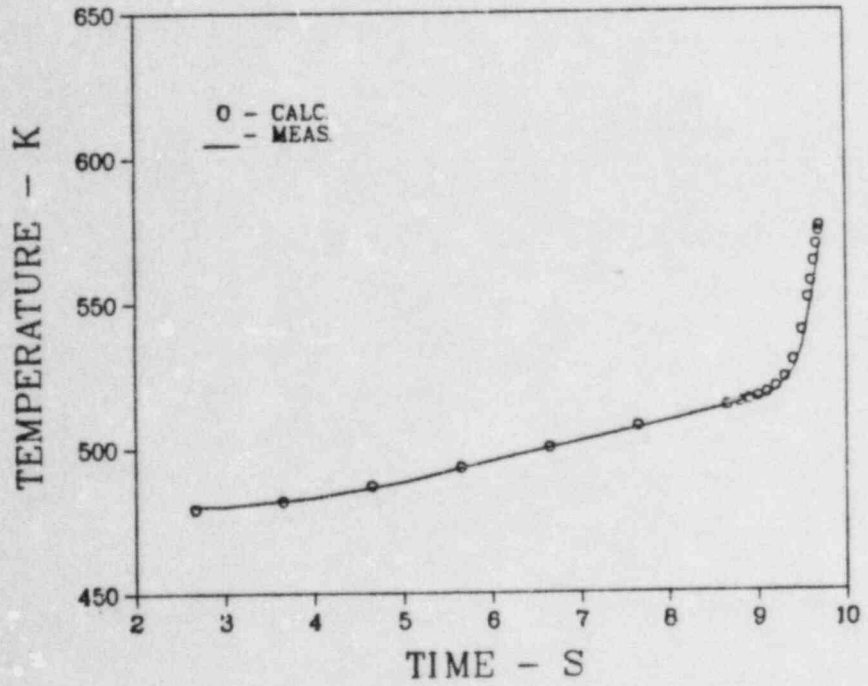

Fig. A16. Comparison of observed and predicted temperatures for HEDL test HUT-37B at an axial location 12.7 mm (0.5 in.) above the bottom of the fuel column.

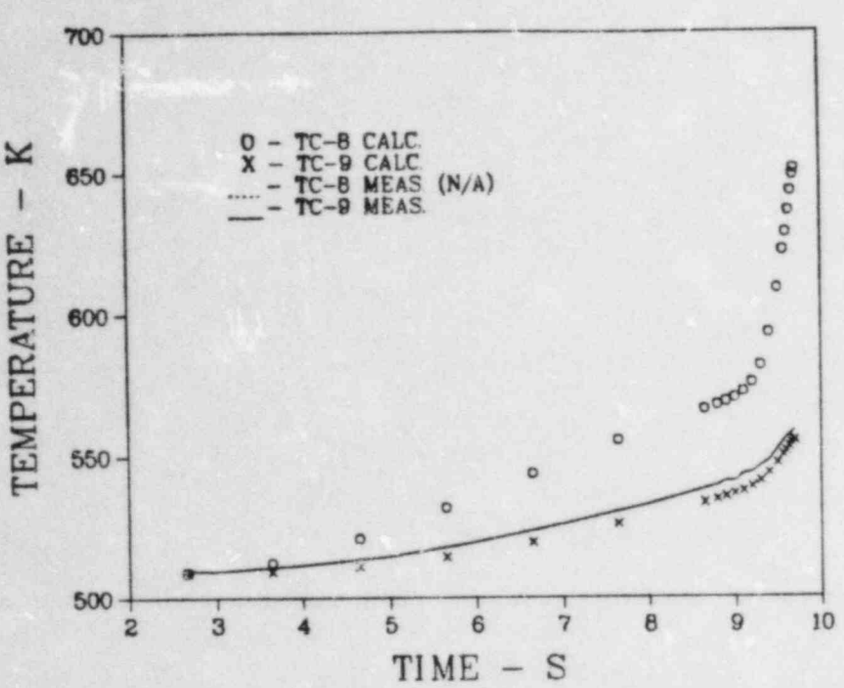

Fig. A17. Comparison of observed and predicted temperatures for HEDL test HUT-37B at an axial location 63.5 mm (2.5 in.) above the bottom of the fuel column.

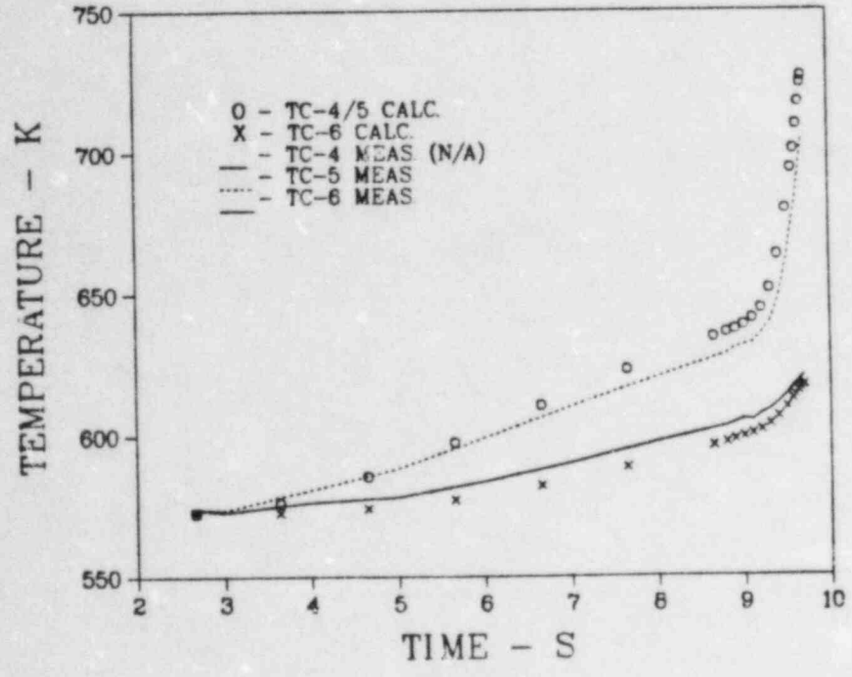

Fig. A18. Comparison of observed and predicted temperatures for HEDL test HUT-37B at axial midplane of the fuel column.

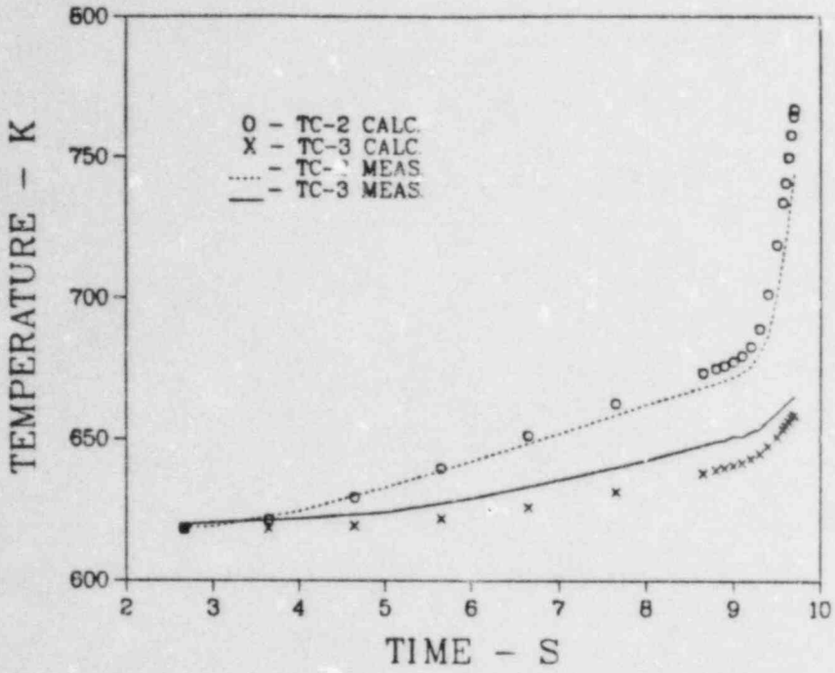

Fig. A19. Comparison of observed and predicted temperatures for HEDL test HUT-37B at an axial location 279 mm (11 in.) above the bottom of the fuel column.

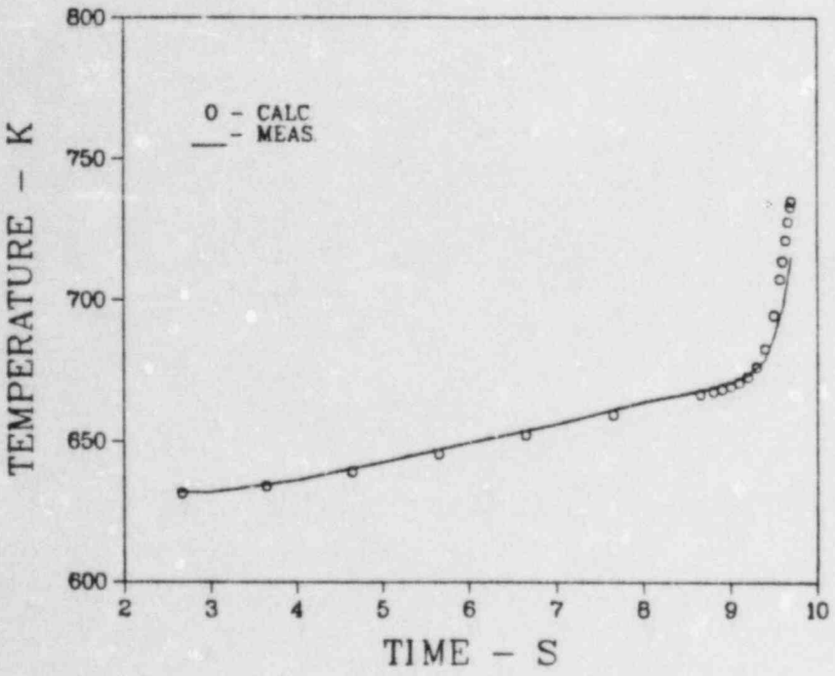

Fig. A20. Comparison of observed and predicted temperatures for HEDL test HUT-37B at an axial location 330 mm (13 in.) above the bottom of the fuel column.

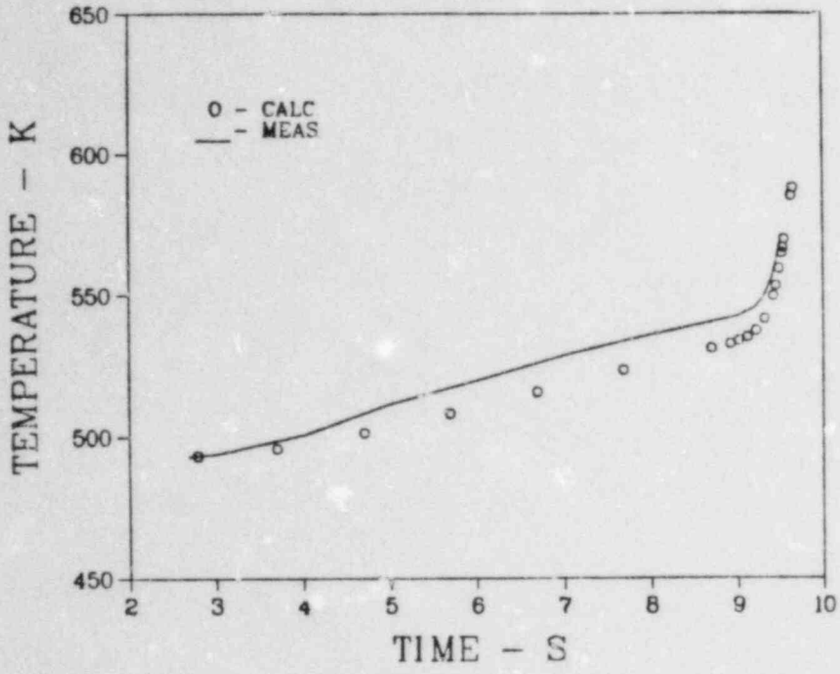

Fig. A21. Comparison of observed and predicted temperatures for HEDL test HUT-36B at an axial location 12.7 mm (0.5 in.) above the bottom of the fuel column.

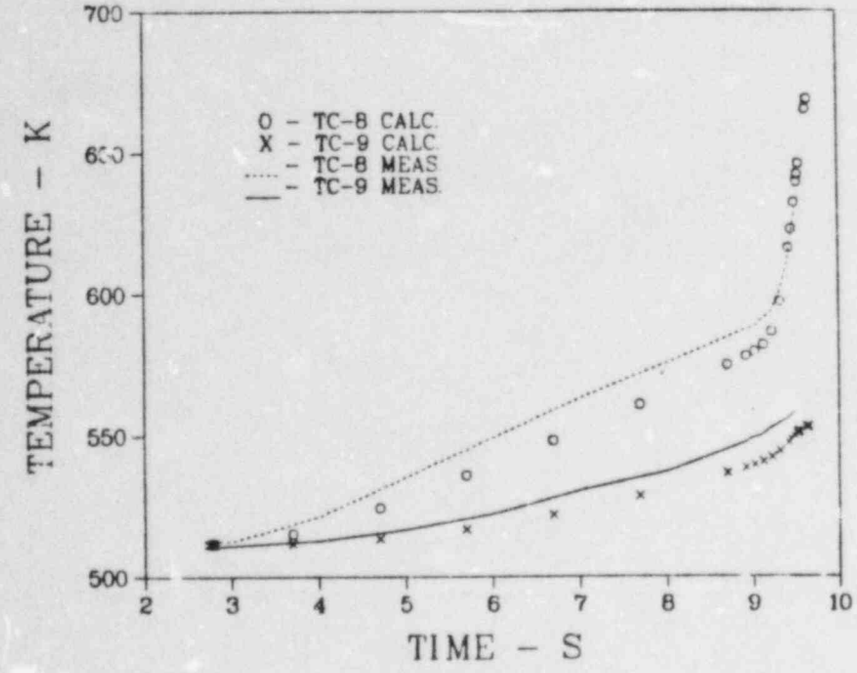

Fig. A22. Comparison of observed and predicted temperatures for HEDL test HUT-36B at an axial location 63.5 mm (2.5 in.) above the bottom of the fuel column.

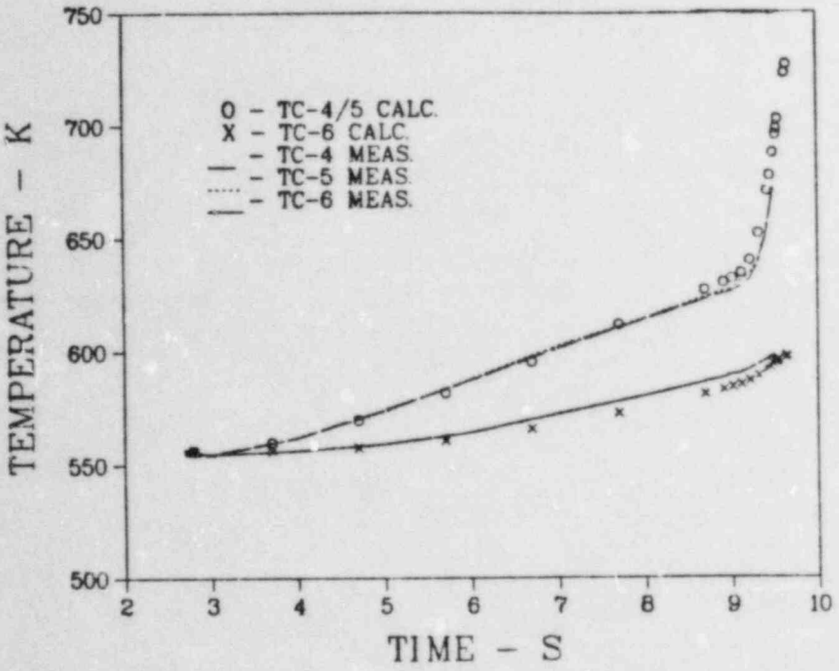

Fig. A23. Comparison of observed and predicted temperatures for HEDL test HUT-36B at axial midplane of the fuel column.

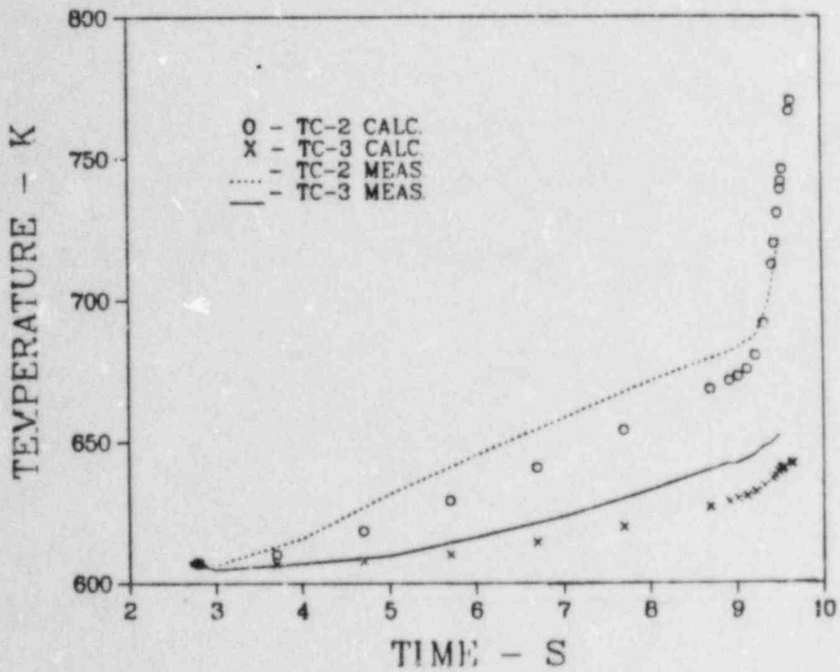

Fig. A24. Comparison of observed and predicted temperatures for HEDL test HUT-36B at an axial location 279 mm (11 in.) above the bottom of the fuel column.

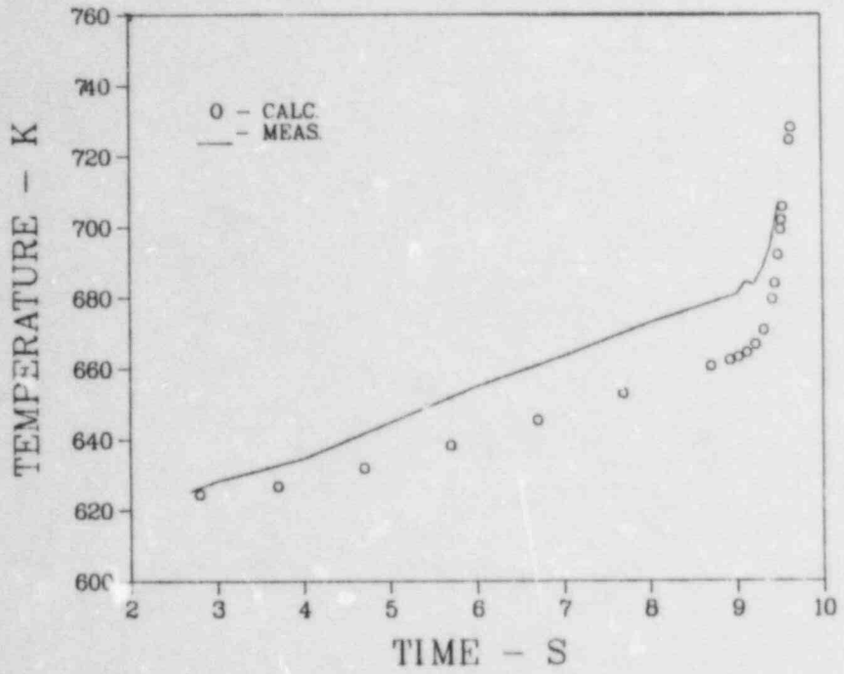

Fig. A25. Comparison of observed and predicted temperatures for HEDL test HUT-36B at an axial location 330 mm (13 in.) above the bottom of the fuel column.

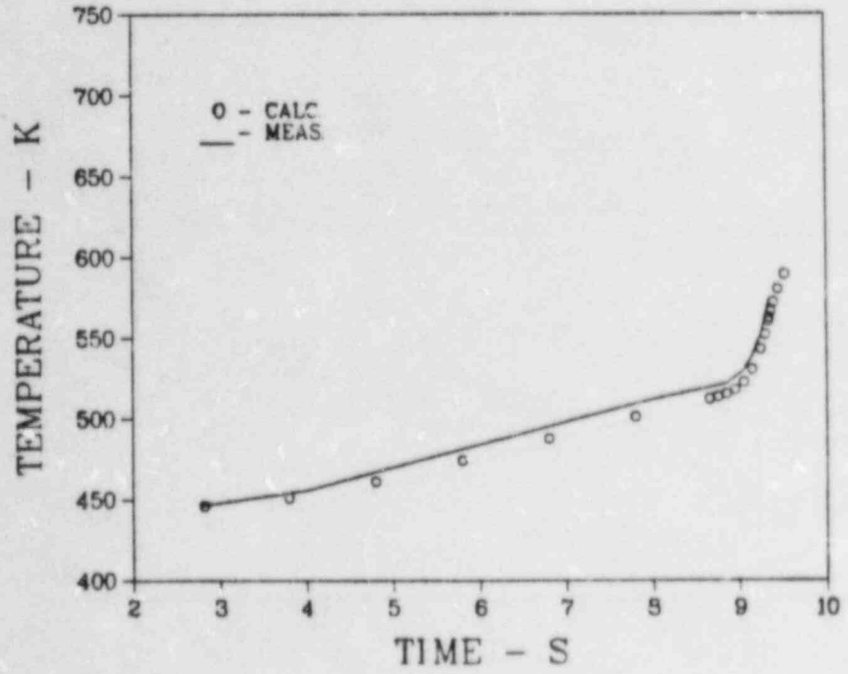

Fig. A26. Comparison of observed and predicted temperatures for HEDL test HUT-32A at an axial location 12.7 mm (0.5 in.) above the bottom of the fuel column.

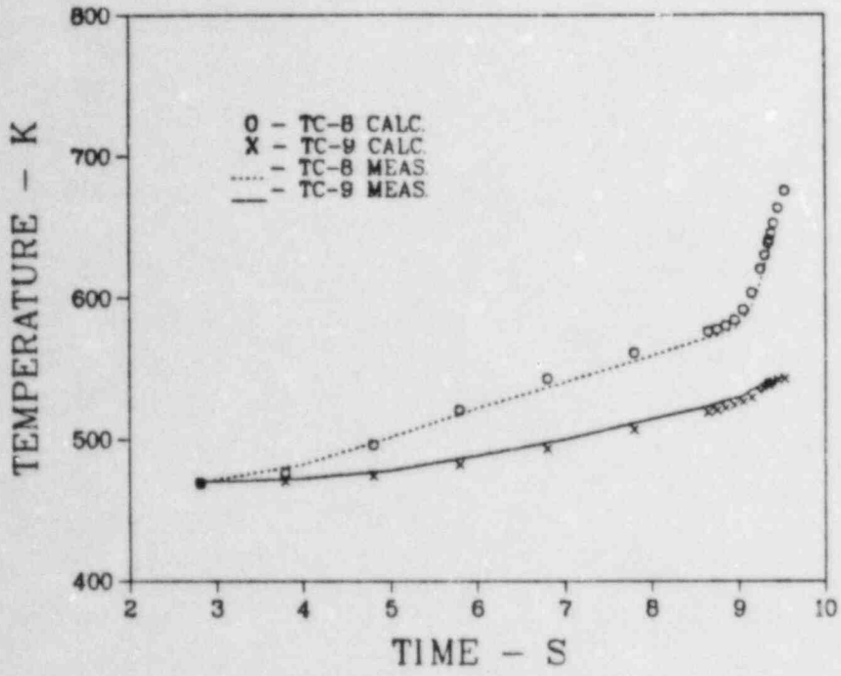

Fig. A27. Comparison of observed and predicted temperatures for HEDL test HUT-32A at an axial location 63.5 mm (2.5 in.) above the bottom of the fuel column.

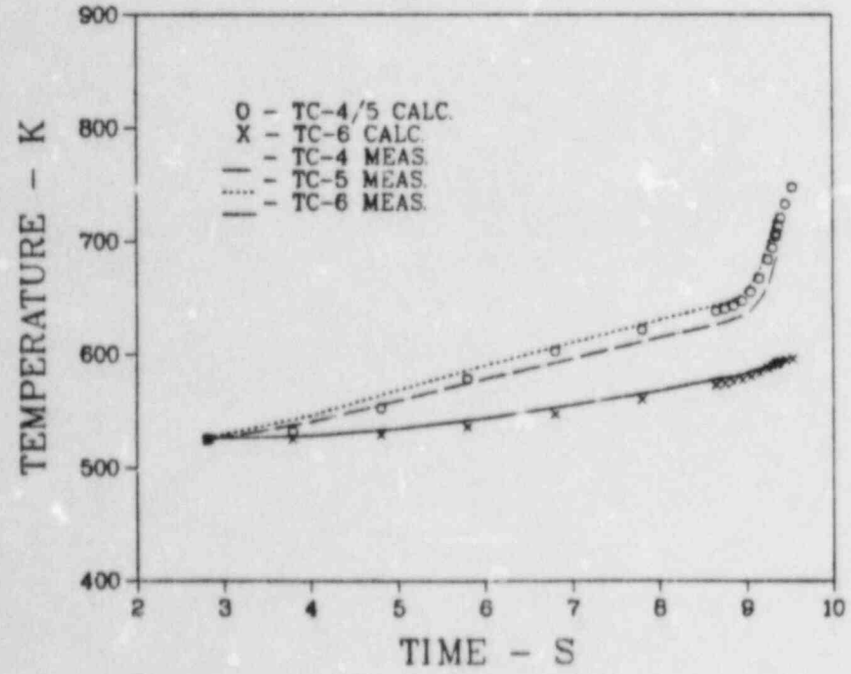

Fig. A28. Comparison of observed and predicted temperatures for HEDL test HUT-32A at axial midplane of the fuel column.

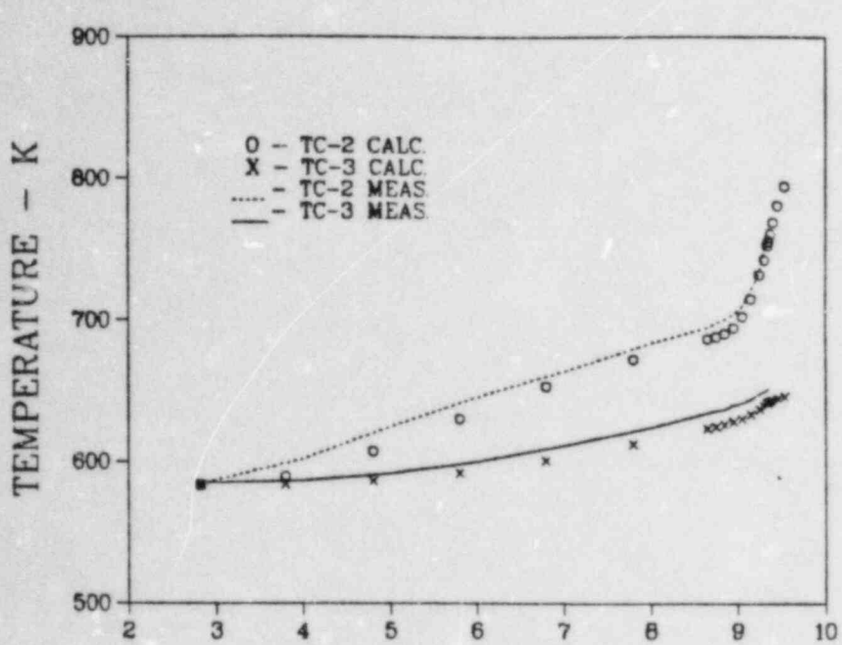

Fig. A29. Comparison of observed and predicted temperatures for HEDL test HUT-32A at an axial location 279 mm (11 in.) above the bottom of the fuel column.

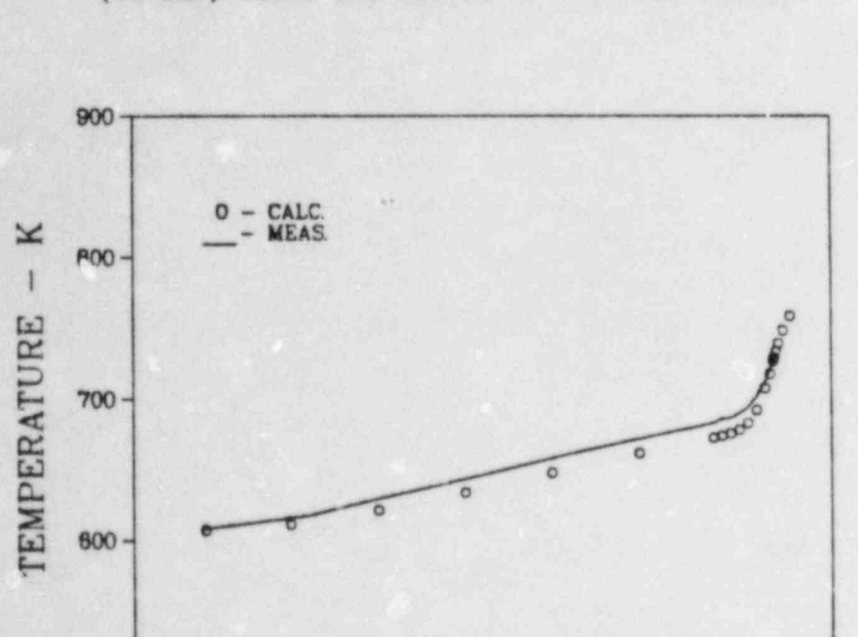

Fig. A30. Comparison of observed and predicted temperatures for HEDL test HUT-32A at an axial location 330 mm (13 in.) above the bottom of the fuel column.

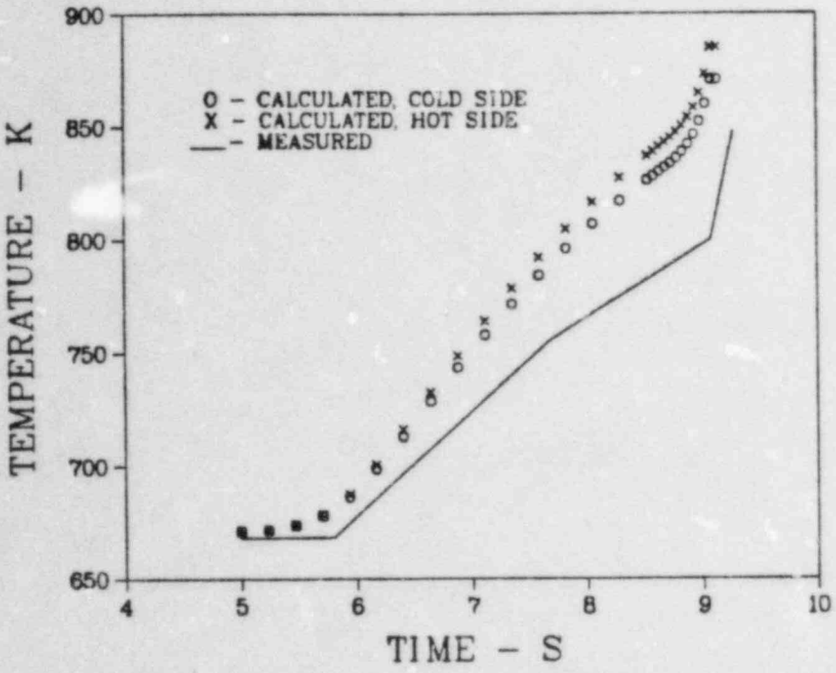

Fig. A31. Comparison of observed and predicted temperatures for HEDL test HUT-57B at an axial location 12.7 mm (0.5 in.) above the bottom of the fuel column.

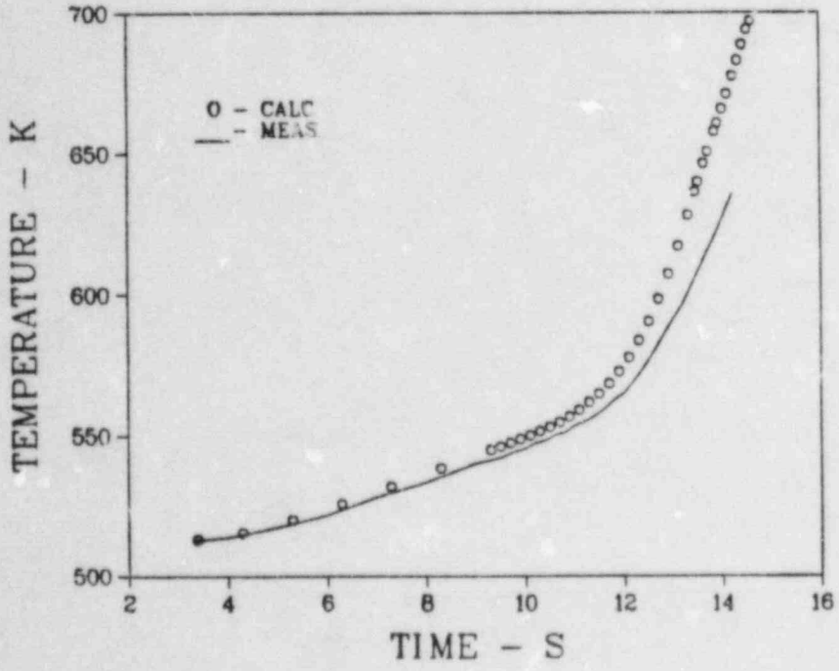

Fig. A32. Comparison of observed and predicted temperatures for HEDL test HUT-57B at an axial location 63.5 mm (2.5 in.) above the bottom of the fuel column.

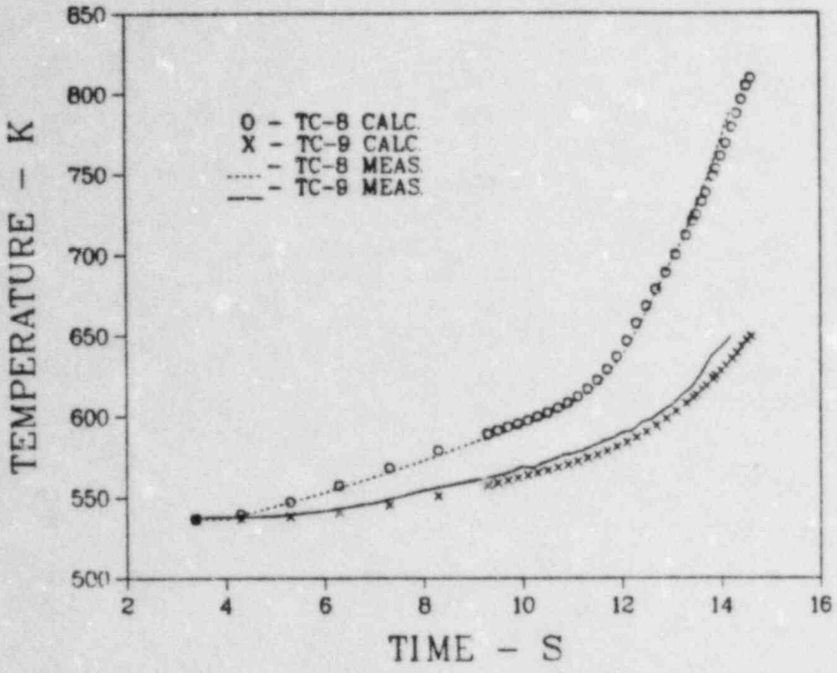

Fig. A33. Comparison of observed and predicted temperatures for HEDL test HUT-57B at axial midplane of the fuel column.

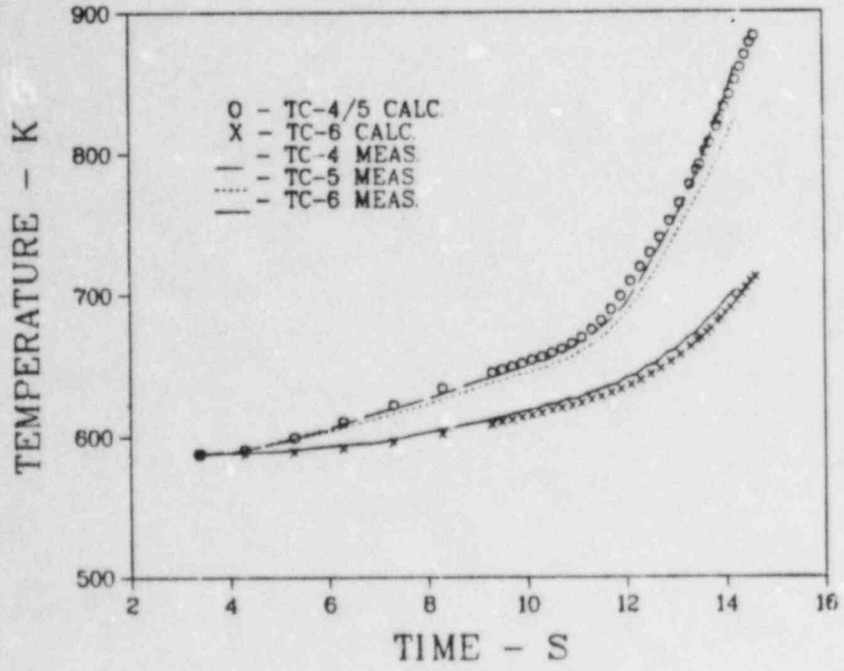

Fig. A34. Comparison of observed and predicted temperatures for HEDL test HUT-57B at an axial location 279 mm (11 in.) above the bottom of the fuel column.

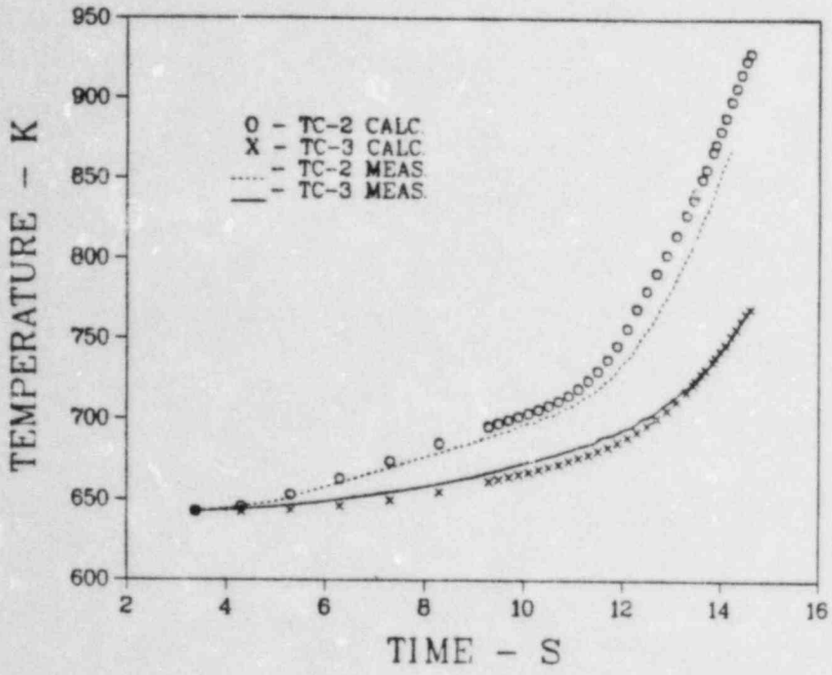

Fig. A35. Comparison of observed and predicted temperatures for HEDL test HUT-57B at an axial location 330 mm (13 in.) above the bottom of the fuel column.

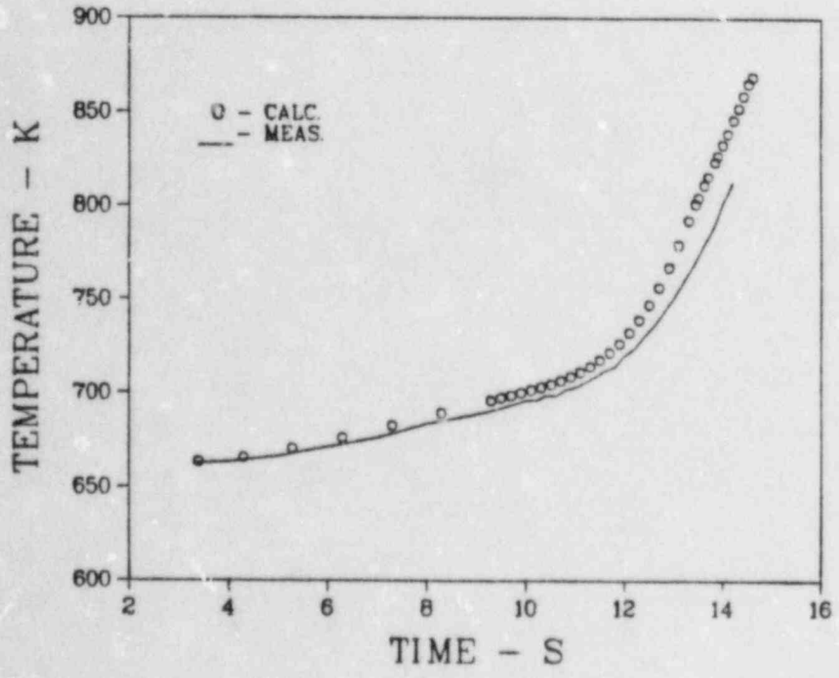

Fig. A36. Comparison of observed and predicted temperatures for HEDL test HUT-55A at an axial location 12.7 mm (0.5 in.) above the bottom of the fuel column.

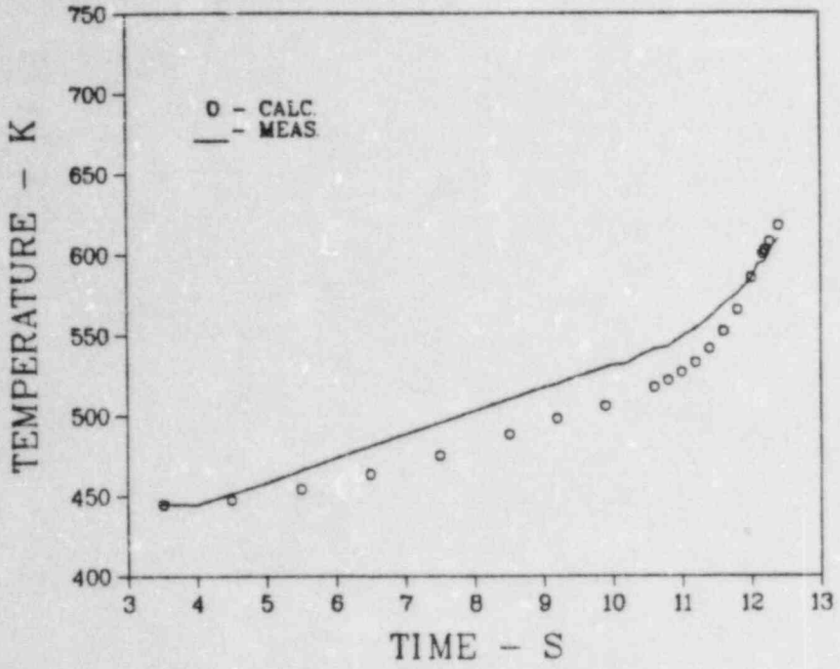

Fig. A37. Comparison of observed and predicted temperatures for HEDL test HUT-55A at an axial location 63.5 mm (2.5 in.) above the bottom of the fuel column.

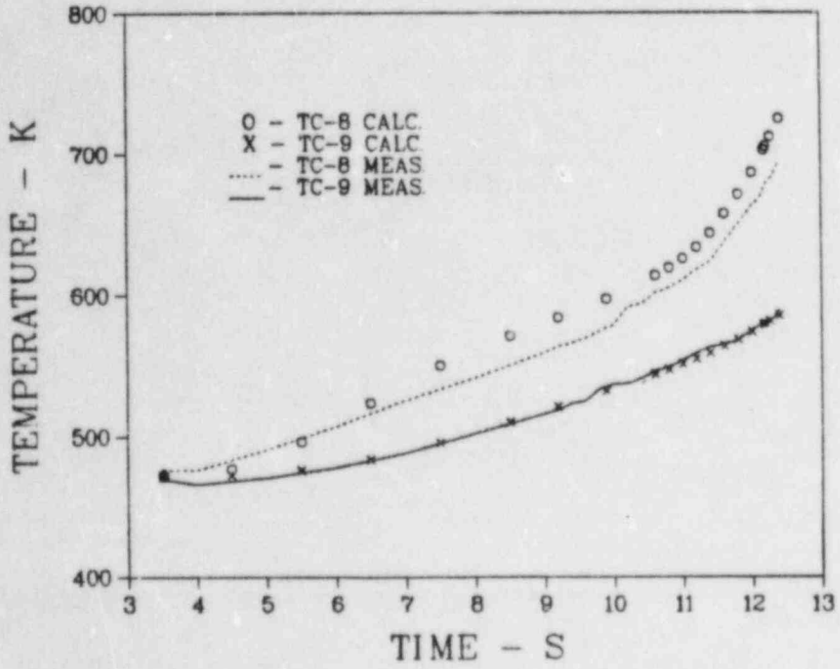

Fig. A38. Comparison of observed and predicted temperatures for HEDL test HUT-55A at axial midplane of the fuel column.

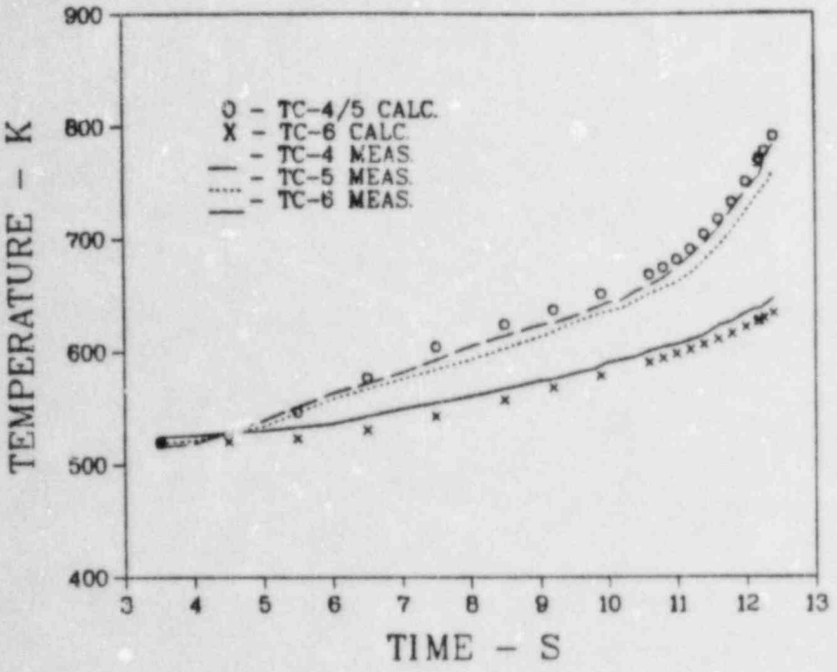

Fig. A39. Comparison of observed and predicted temperatures for HEDL test HUT-55A at an axial location 279 mm (11 in.) above the bottom of the fuel column.

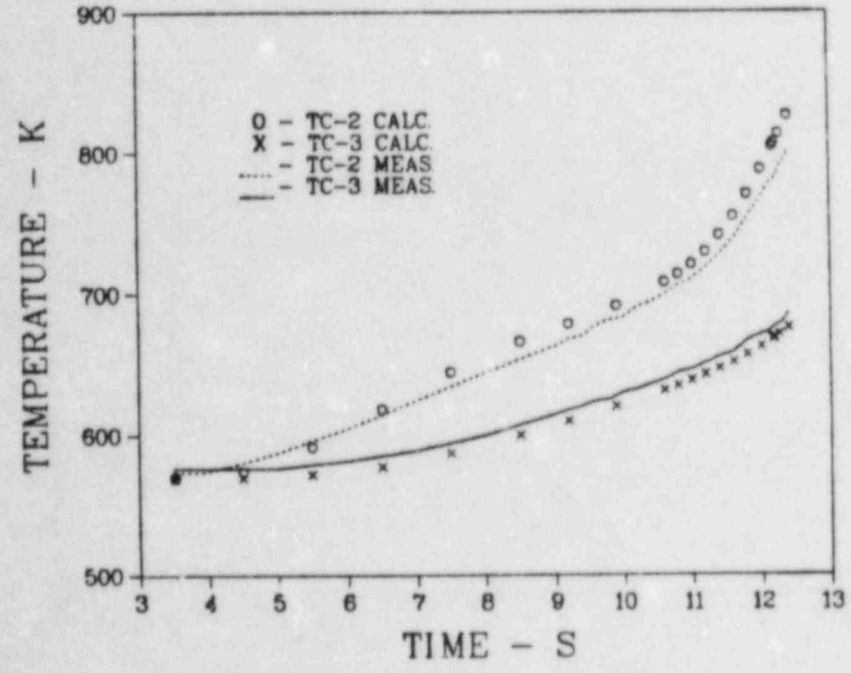

Fig. A40. Comparison of observed and predicted temperatures for HEDL test HUT-55A at an axial location 330 mm (13 in.) above the bottom of the fuel column.

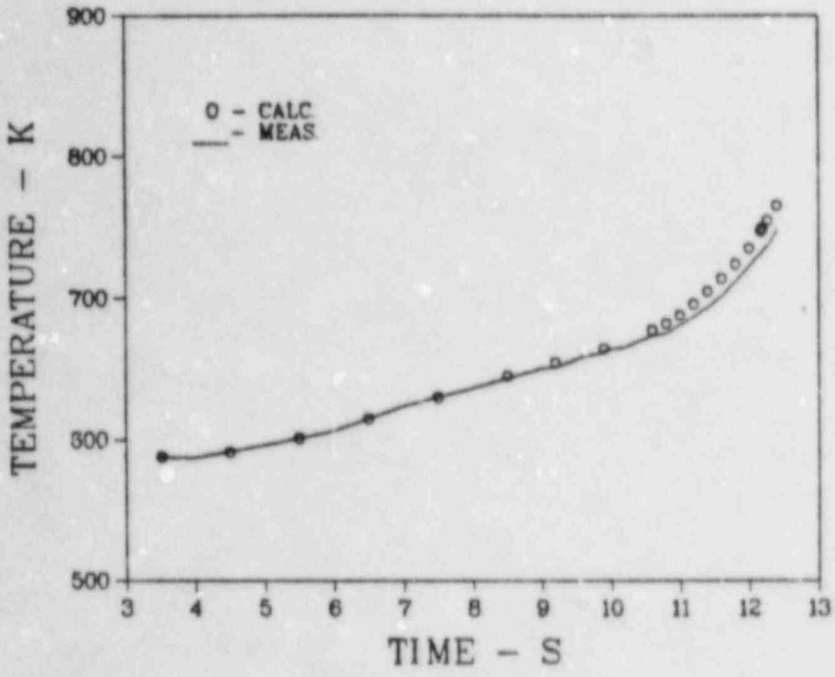

Fig. A41. Comparison of observed and predicted temperatures for HEDL test HUT-52B at an axial location 12.7 mm (0.5 in.) above the bottom of the fuel column.

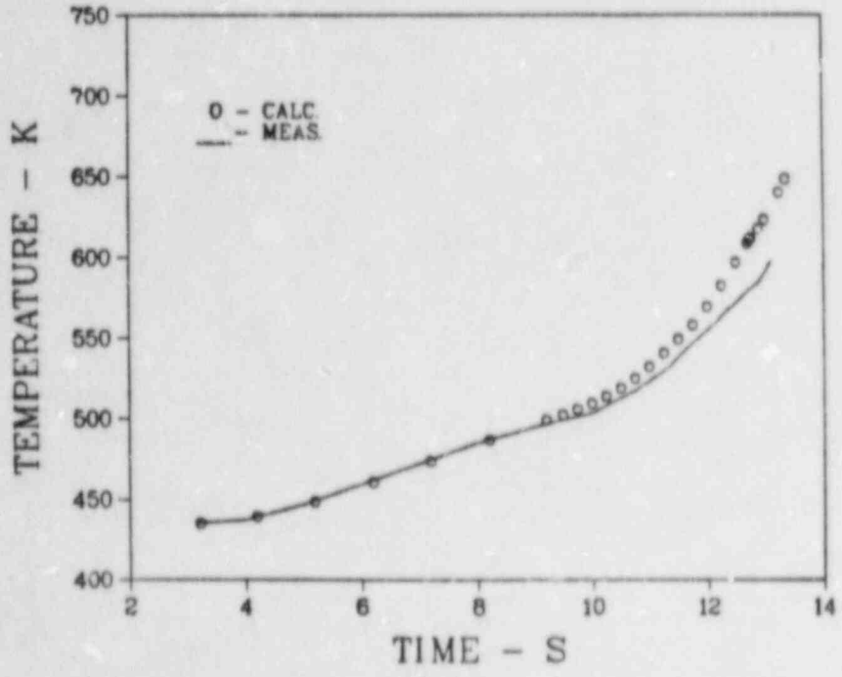

Fig. A42. Comparison of observed and predicted temperatures for HEDL test HUT-52B at an axial location 63.5 mm (2.5 in.) above the bottom of the fuel column.

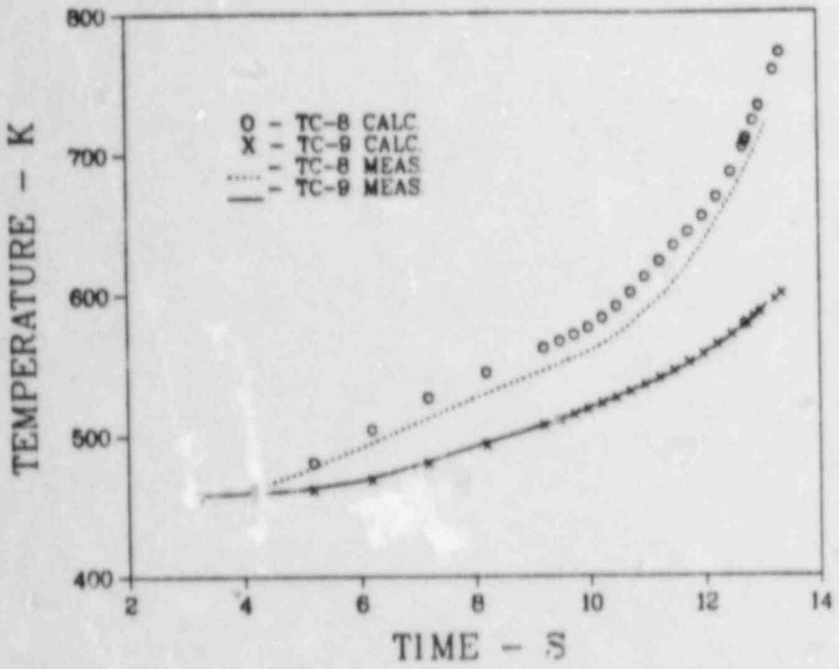

Fig. A43. Comparison of observed and predicted temperatures for HEDL test HUT-52B at axial midplane of the fuel column.

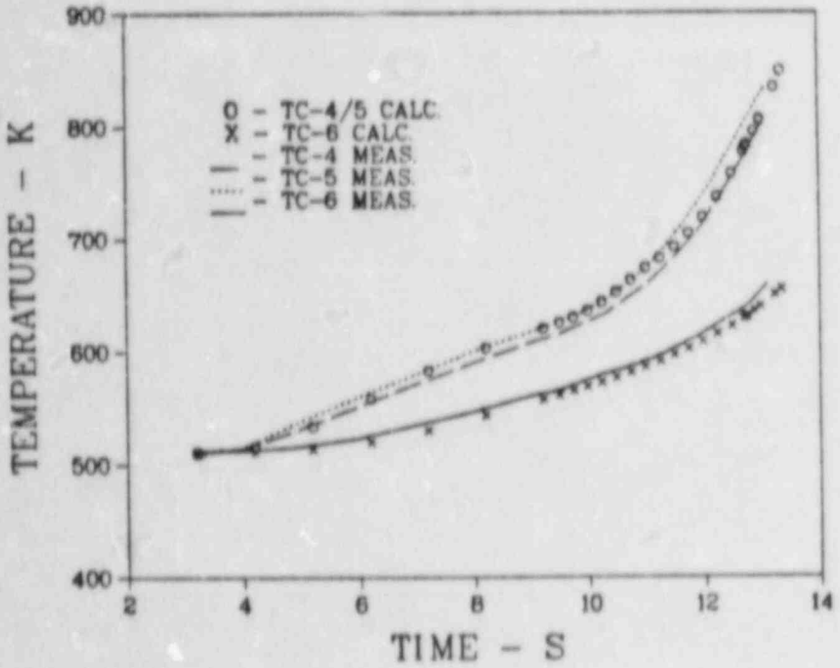

Fig. A44. Comparison of observed and predicted temperatures for HEDL test HUT-52B at an axial location 279 mm (11 in.) above the bottom of the fuel column.

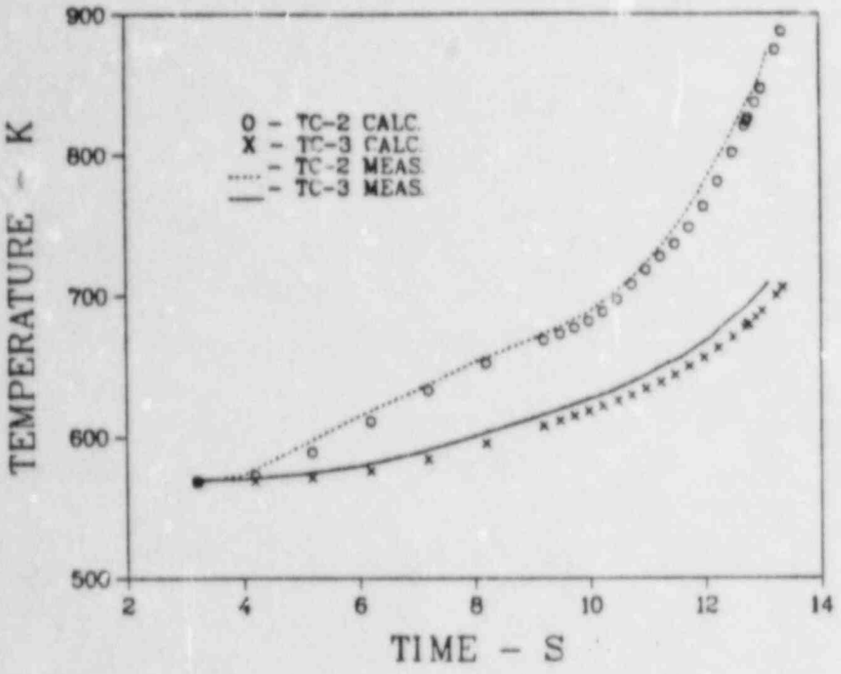

Fig. A45. Comparison of observed and predicted temperatures for HEDL test HUT-52B at an axial location 330 mm (13 in.) above the bottom of the fuel column.

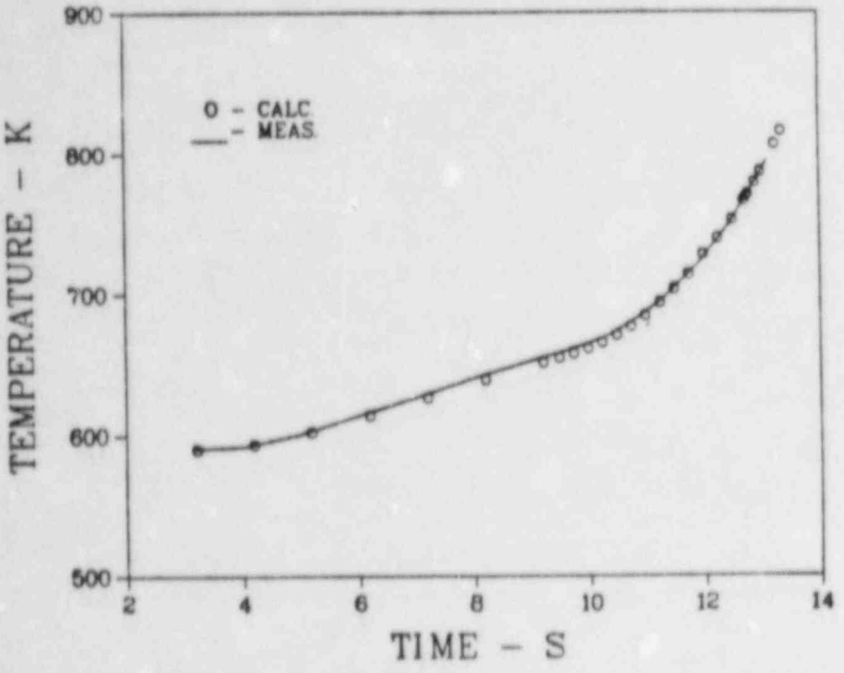

Fig. A46. Comparison of observed and predicted outlet coolant temperatures for ANL test E6 at an axial location 343 mm (13.5 in.) above the top of the fuel column.

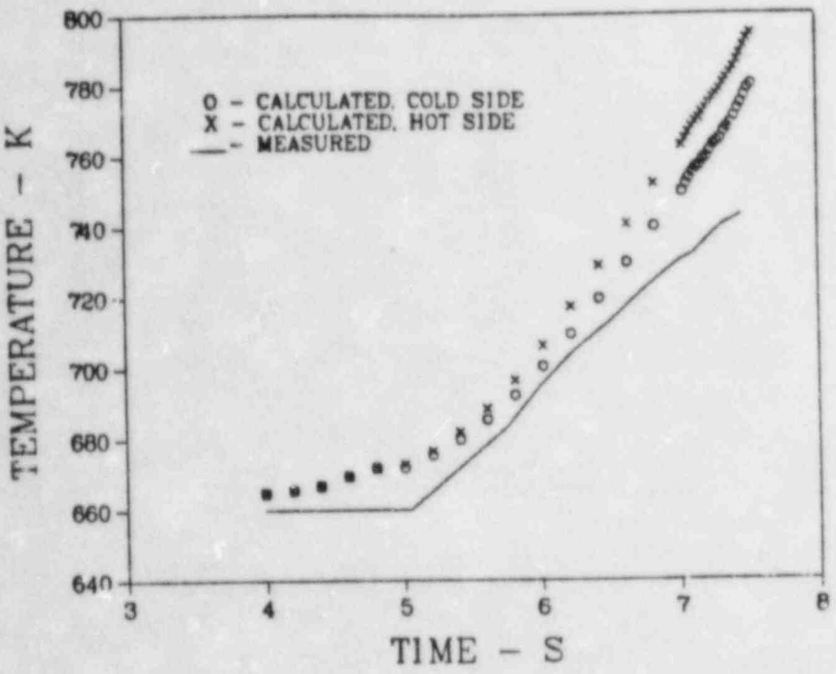

Fig. A47. Comparison of observed and predicted outlet coolant temperatures for ANL test E7 at an axial location 660 mm (26 in.) above the top of the fuel column.

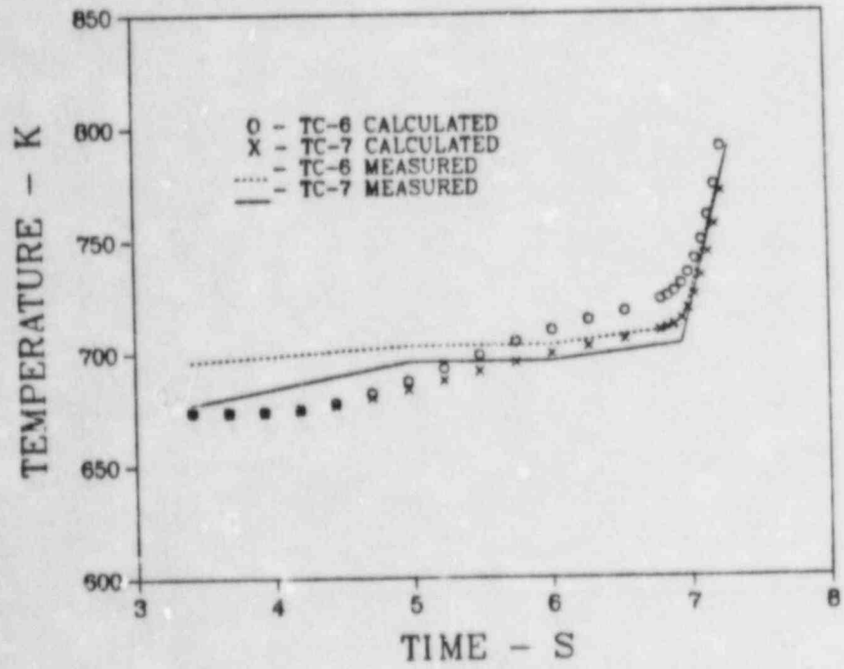

Fig. A48. Comparison of observed and predicted fluted tube temperatures for ANL test E8 at axial midplane of the fuel column.

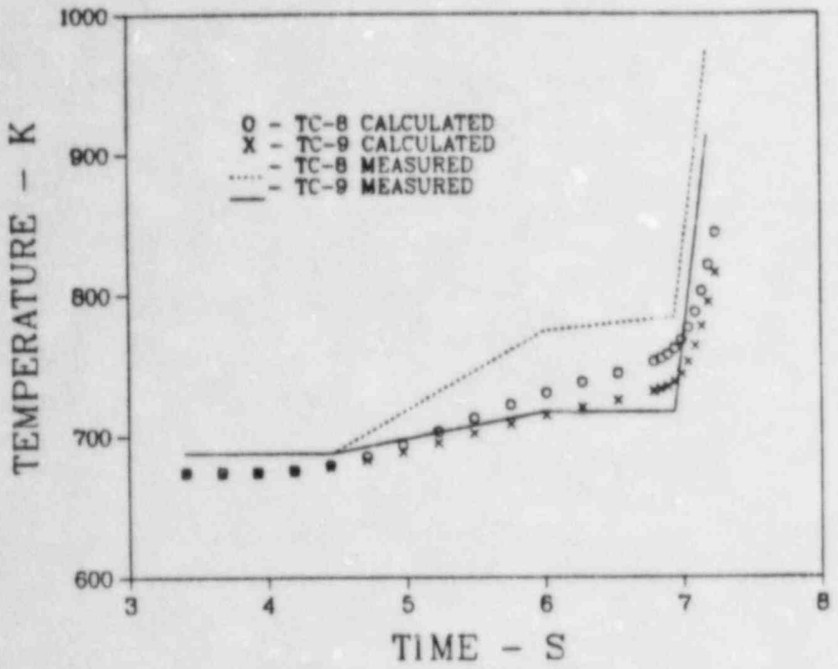

Fig. A49. Comparison of observed and predicted fluted tube temperatures for ANL test E8 at an axial location 279 mm (11 in.) above the bottom of the fuel column.

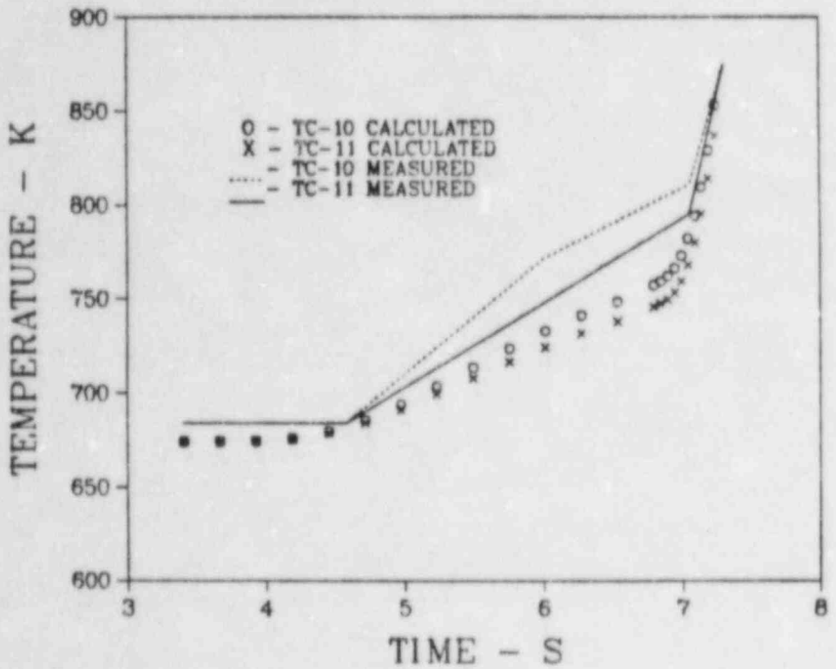

Fig. A50. Comparison of observed and predicted fluted tube temperatures for ANL test E8 at the top of the fuel column.

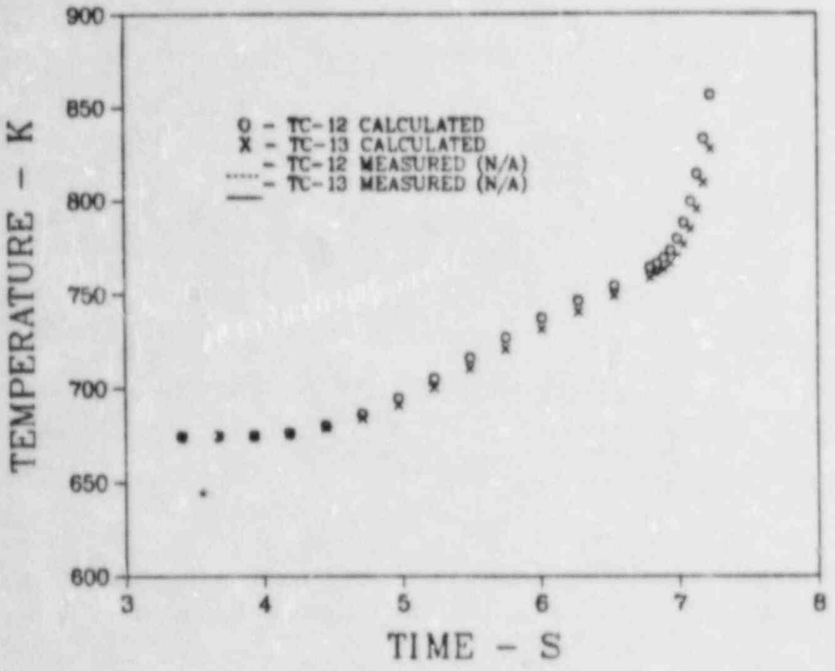

Fig. A51. Comparison of observed and predicted fluted tube temperatures for ANL test E3 at axial locations 368 to 470 mm (14.5 to 18.5 in.) above the top of the fuel column.

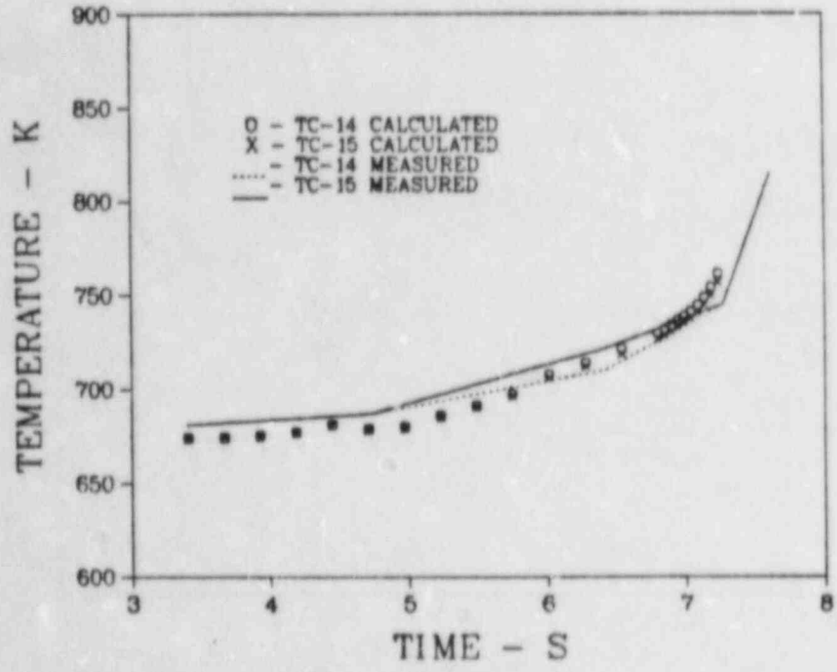

Fig. A52. Comparison of observed and predicted coolant outlet temperatures for ANL test E8 at an axial location 1211 mm (48 in.) above the top of the fuel column.

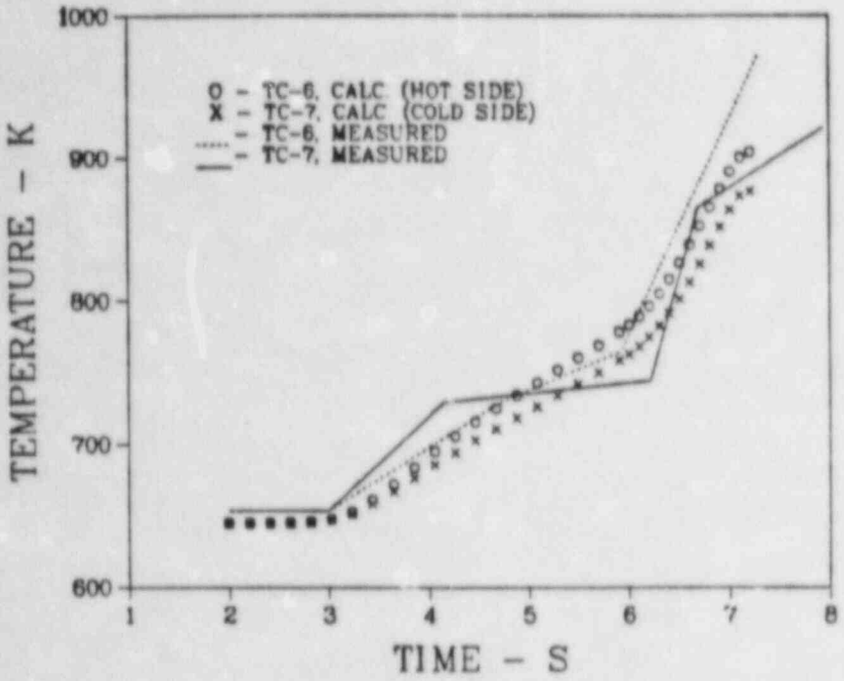

Fig. A53. Comparison of observed and predicted fluted tube temperatures for ANL test H4 at axial midplane of the fuel column.

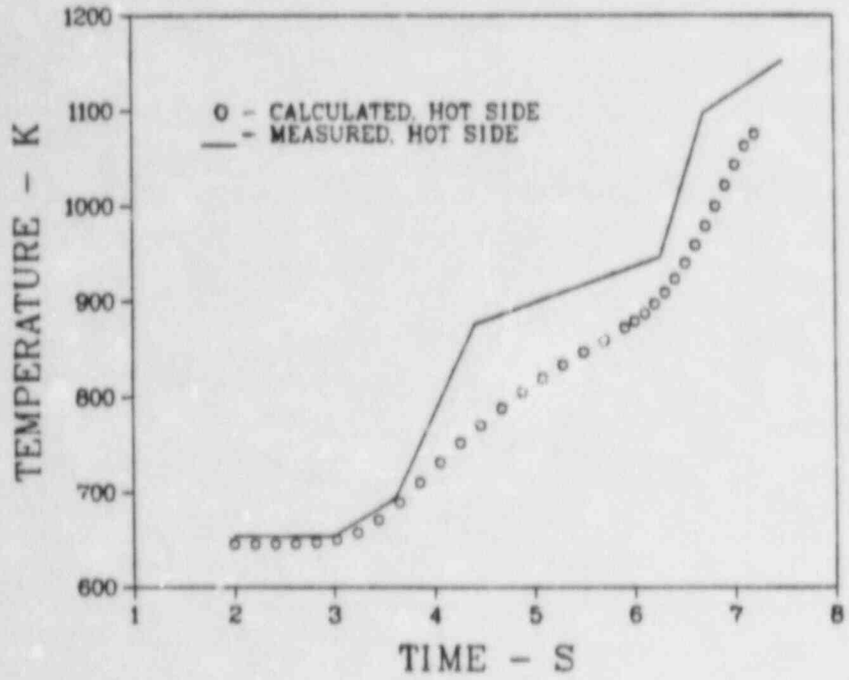

Fig. A54. Comparison of observed and predicted fluted tube temperatures for ANL test H4 at the top of the fuel column.

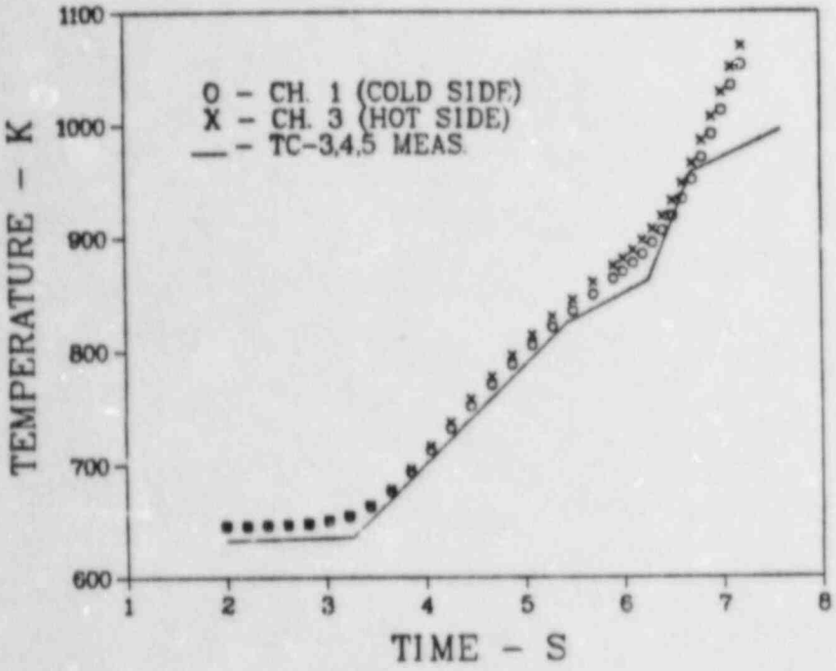

Fig. A55. Comparison of observed and predicted coolant outlet temperatures for ANL test H4 at an axial location 343 mm (13.5 in.) above the top of the fuel column.

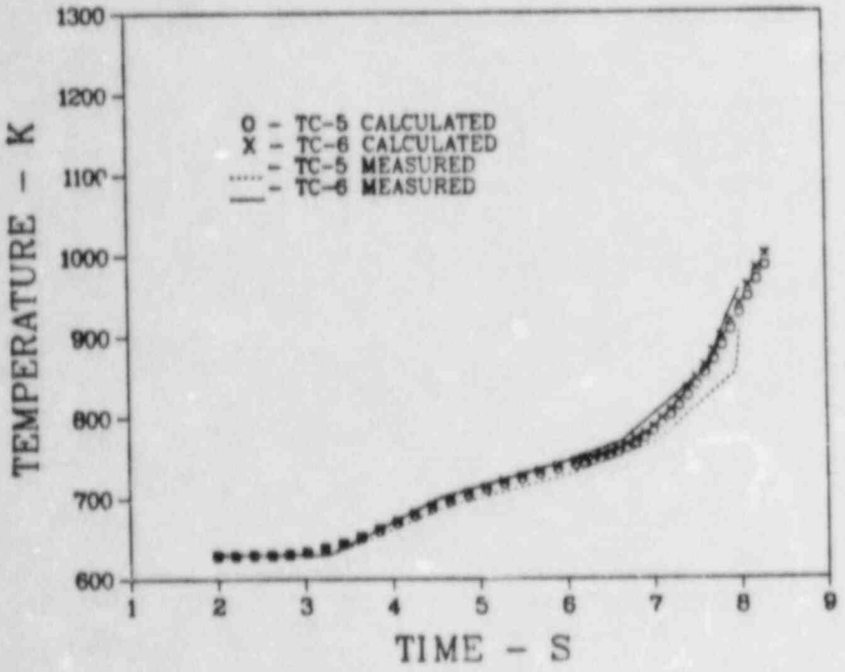

Fig. A56. Comparison of observed and predicted coolant outlet temperatures for ANL test H5 at an axial location 343 mm (13.5 in.) above the top of the fuel column.

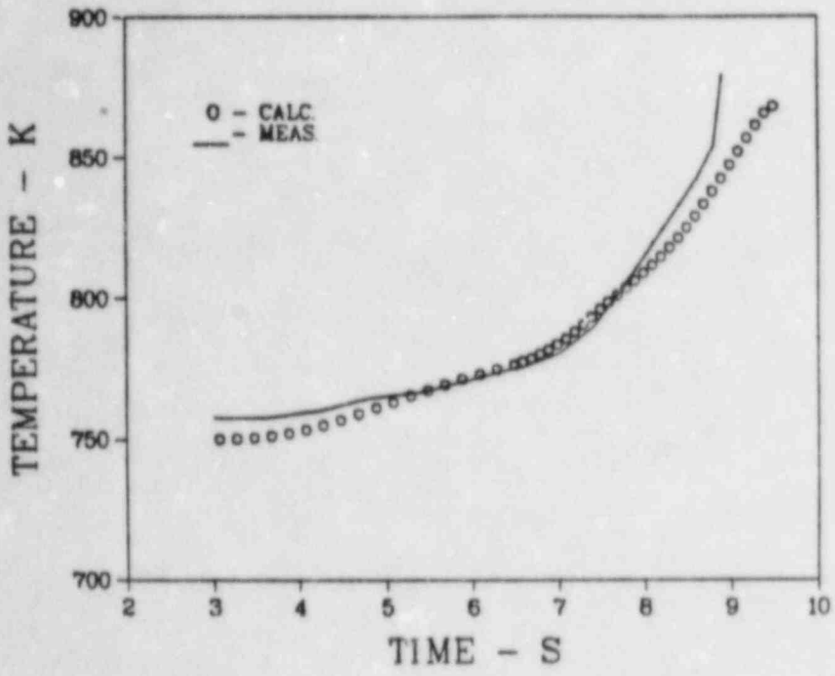

Fig. A57. Comparison of observed and predicted fluted tube temperatures for ANL test H6 at axial midplane of the fuel column.

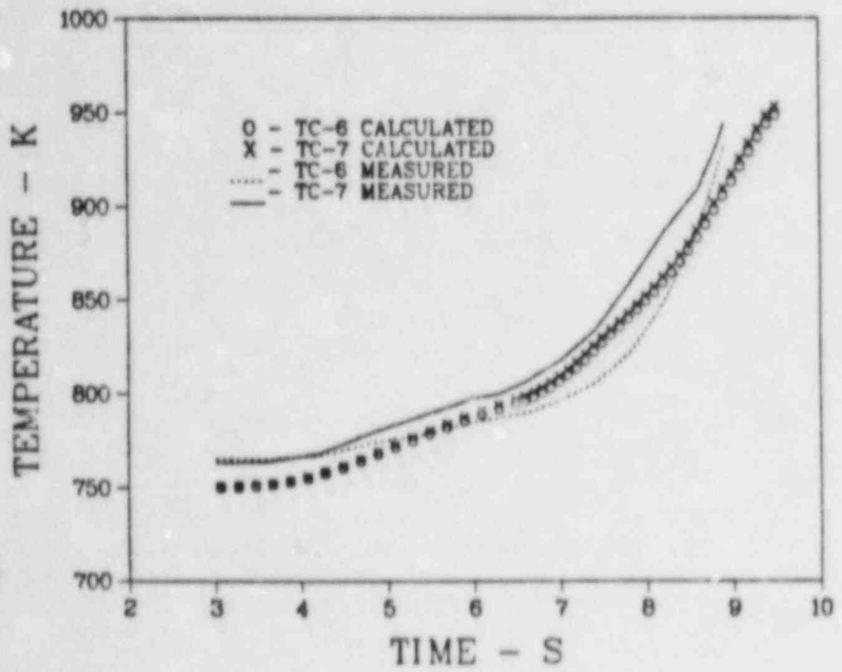

Fig. A58. Comparison of observed and predicted fluted tube temperatures for ANL test H6 at an axial location 279 mm (11 in.) above the bottom of the fuel column.

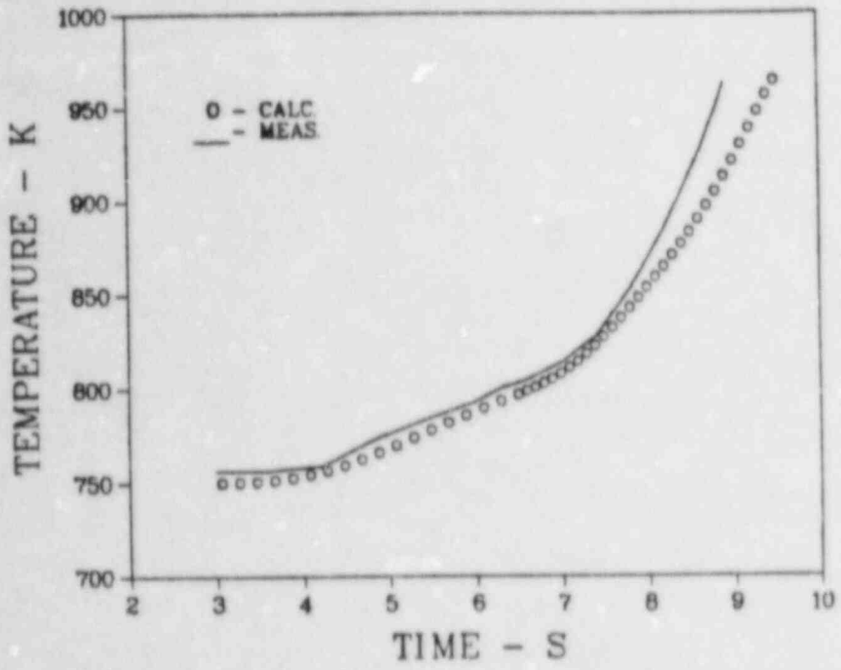

Fig. A59. Comparison of observed and predicted fluted tube temperatures for ANL test H6 at an axial location 254 mm (10 in.) above the top of the fuel column.

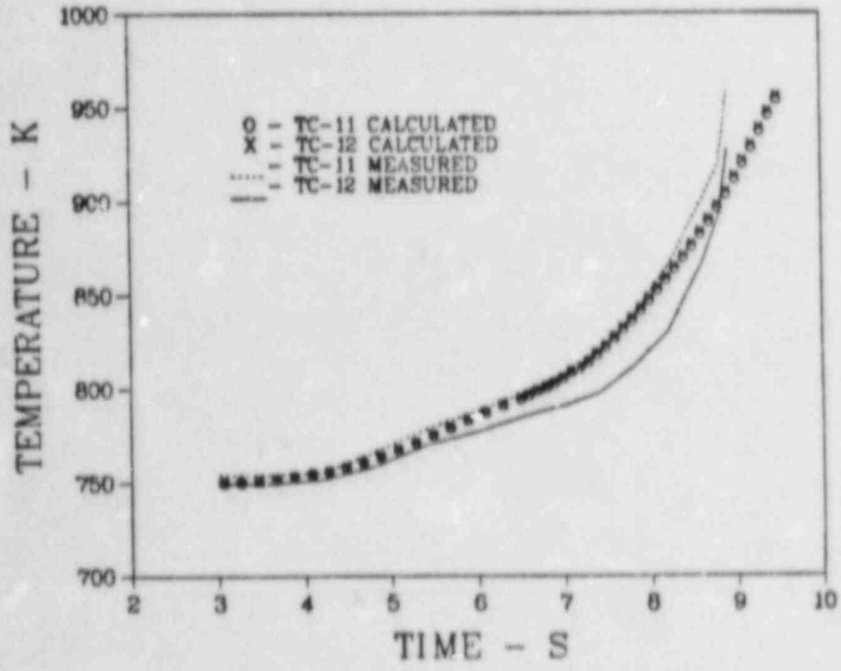

Fig. A60. Comparison of observed and predicted outlet coolant temperatures for ANL test H6 at an axial location 1211 m (48 in.) above the top of the fuel column.

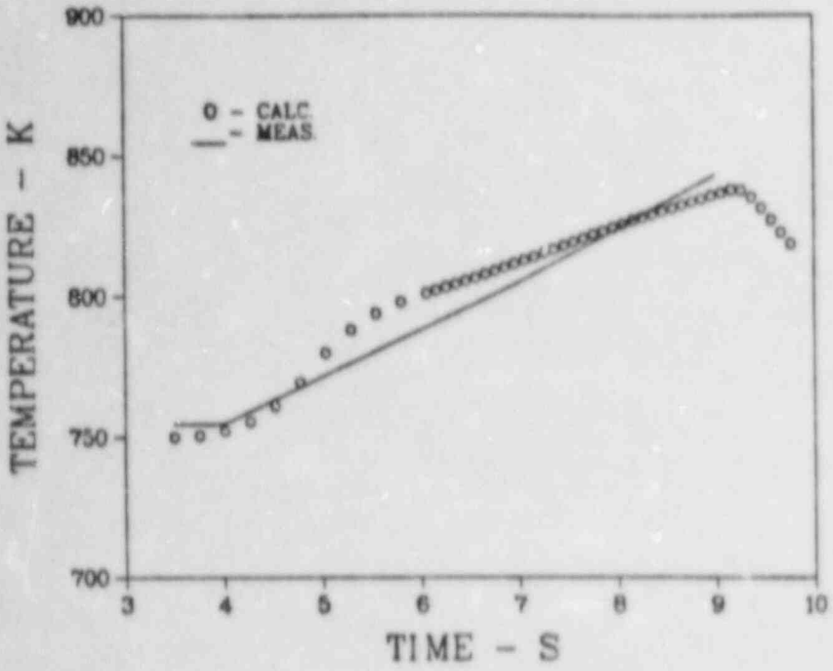

Fig. A61. Comparison of observed and predicted outlet coolant temperatures for ANL test J1 at axial midplane of the fuel column.

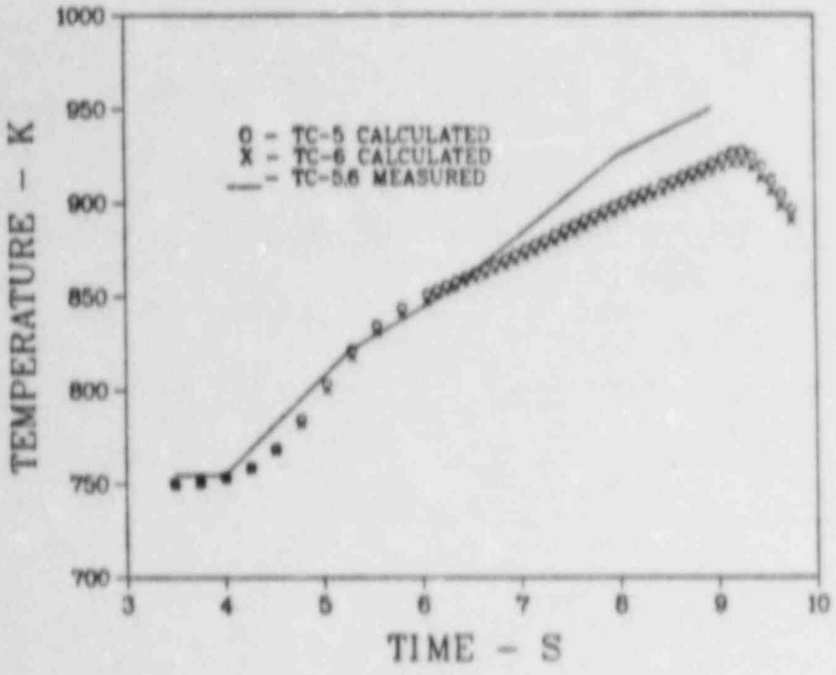

Fig. A62. Comparison of observed and predicted outlet coolant temperatures for ANL test J1 at the top of the fuel column.

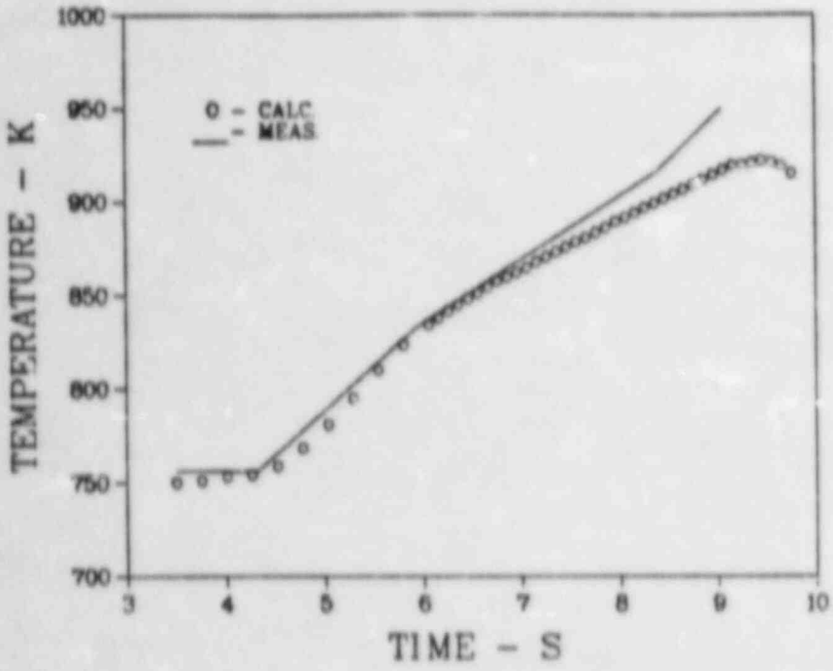

Fig. A63. Comparison of observed and predicted coolant outlet temperatures for ANL test J1 at an axial location 1211 mm (48 in.) above the top of the fuel column.

DISTRIBUTION

	Copies
Nuclear Regulatory Commission, R7, Bethesda, Maryland	248
Technical Information Center, Oak Ridge, Tennessee	2
Los Alamos National Laboratory, Los Alamos, New Mexico	50
	300

NRC FORM 335 (16-83) U.S. NUCLEAR REGULATORY COMMISSION

BIBLIOGRAPHIC DATA SHEET

1. REPORT NUMBER (Assigned by TIDC, add Vol. No., if any)
NUREG/CR-3679
LA-10041-MS

2. Leave blank

3. TITLE AND SUBTITLE
Calibration and Qualification of the Los Alamos Failure Model (LAFM)

4. RECIPIENT'S ACCESSION NUMBER

5. DATE REPORT COMPLETED
MONTH: February YEAR: 1984

6. AUTHOR(S)
Ralph E. Baars

7. DATE REPORT ISSUED
MONTH: May YEAR: 1984

8. PERFORMING ORGANIZATION NAME AND MAILING ADDRESS (Include Zip Code)
Los Alamos National Laboratory
Los Alamos, New Mexico 87545

9. PROJECT/TASK/WORK UNIT NUMBER

10. FIN NUMBER
A7015

11. SPONSORING ORGANIZATION NAME AND MAILING ADDRESS (Include Zip Code)
Division of Accident Evaluation
Office of Regulatory Research
U.S. Nuclear Regulatory Commission
Washington, DC 20555

12a. TYPE OF REPORT
Informal

12b. PERIOD COVERED (Inclusive dates)

13. SUPPLEMENTARY NOTES

14. ABSTRACT (200 words or less)

The analysis procedure is described in detail for use of the LAFM computer code to predict LMFBR fuel pin performance under transient overpower conditions; also, 5 tests for calibration and 13 tests for qualification are analyzed. The times of cladding breach (molten fuel expulsion) were predicted with an average relative error of 5 per cent. An enthalpy of 1112 kJ/kg correlated the peak fuel enthalpies at the time of failure with a standard deviation of 98 kJ/kg. We conclude with a discussion that many varied tests must be analyzed for adequate evaluation of a fuel pin performance code.

15a. KEY WORDS AND DOCUMENT ANALYSIS

15b. DESCRIPTORS

16. AVAILABILITY STATEMENT
Unlimited

17. SECURITY CLASSIFICATION (This report)
Unclassified

18. NUMBER OF PAGES

19. SECURITY CLASSIFICATION (This page)
Unclassified

20. PRICE
$

☆U.S. GOVERNMENT PRINTING OFFICE: 1984-0-776-026/4067

Available from

GPO Sales Program
Division of Technical Information and Document Control
US Nuclear Regulatory Commission
Washington, DC 20555

and

National Technical Information Service
Springfield, VA 22161

Los Alamos